Full-Field Strain and Temperature Measurement of Epoxy Resin PR-520 Subjected to Tensile Loading at Various Strain Rates

Undergraduate Honors Thesis

Submitted to the Department of Mechanical and Aerospace Engineering
The Ohio State University

In Partial Fulfillment of the Requirements
For Graduation with Distinction
in Aeronautical Engineering

Mark Joseph Konieczny
May, 2018

ABSTRACT

Increasingly, aircraft engine manufacturers are turning towards composite materials for use in various engine components; more specifically the fan case surrounding the engine. The high strength, high stiffness, and low weight of composites make them a competitive alternative to traditional aircraft materials such as aluminum and titanium. Composites in fan case applications have become an important topic of research because regulations require that an aircraft engine case must be able to contain debris resulting from a blade out type engine failure. Once the impact characteristics of these composite materials are determined, a blade out engine failure can be simulated through a computational model, potentially reducing time and cost of designing and manufacturing composite fan cases. The properties of the polymer matrix of the composite become important in impact situations when the force is applied out-of-plane with respect to the composite fibers, and the polymer matrix is the primary factor affecting the strain rate dependency of the composite as a whole. Computational models including the rate dependent effects of the matrix material exist, but they neglect the coupling of the thermal and mechanical responses of the material. The purpose of this study was to simultaneously measure the full field thermal and full field deformation response of epoxy resin PR-520 in tensile tests conducted at strain rates of $0.01s^{-1}$, $1.0s^{-1}$, and $350s^{-1}$. 2-D and 3-D digital image correlation was used for full-field measurement of deformation, and high-speed infrared thermography was used for full-field temperature measurement. The testing was conducted on two test apparatus, a servo-hydraulic load frame for the low and intermediate rate tests, and a direct tension Split-Hopkinson bar for the high rate tests. The results show a coupling between temperature change and strain in

the test specimens, with cooling occurring during elastic deformation, and heating occurring during plastic deformation. The results also show a dependence of both thermal and mechanical response, on strain rate. The data generated by the tests can be used to modify the constitutive equations for the matrix material to allow better prediction of characteristics such as failure strain, strength, and fatigue.

ACKNOWLEDGEMENTS

First and foremost I would like to thank my parents, John and Kathleen Konieczny. Without their guidance and support over the course of my life none of this would have been possible. I would also like to thank my girlfriend Jordan Giesler who has always been understanding of the long hours spent in the lab and the stresses that come with conducting research.

Special thanks to my advisor Dr. Amos Gilat whose support on this project and expertise in the field allowed me to complete this work, as well as for giving me the opportunity to explore this topic. Special thanks also to Dr. Jeremy Seidt who was always available to answer any question I had no matter what he was working on. Thanks to my fellow students and colleagues in the Dynamic Mechanics of Materials lab – Kelton Reiske, Stuart Brand, Yogesh Deshpande, Brian Smith, Nathan Spulak, Elliot Harrod, and Shane Riddle - their collaboration was invaluable and just sitting to talk with them offered a much needed chance to clear my head every now and again. Perhaps most importantly, thanks to Jarrod Smith, who taught me everything I know about infrared thermography and capturing simultaneous full-field strain and temperature measurements. Without his years of experience, and willingness to share his knowledge, this project would never have been completed.

This work was supported by the Federal Aviation Administration in collaboration with the National Aeronautics and Space Administration. Thanks to Robert Goldberg, Gary Roberts, and Joel Johnston at NASA Glenn Research Center for their input and assistance.

TABLE OF CONTENTS

LIST OF FIGURES

LIST OF TABLES

CHAPTER 1: INTRODUCTION

While a desire for more efficient aircraft has driven the need for lighter materials, manufacturers of aircraft components are looking to composites to replace traditional aircraft materials. Boeing has reported that the 787 “Dreamliner”, is comprised of 50% composite materials by weight (Boeing, 2017), and the General Electric, GENx turbofan engine utilizes composites for the engine case as well as the fan blades. In addition to these two companies, there are countless other aircraft component and aircraft engine manufacturers using composites to improve the performance and reduce the weight of their structures.

Composites are traditionally made of two or more materials bonded together; a matrix and a reinforcement of lamina or fibers. The two materials forming a composite can have very different physical and chemical characteristics, but combine to give the whole composite its own unique characteristics. The fibers typically provide high strength and stiffness in the uniaxial direction but are brittle; whereas the matrix usually provides less strength when compared to the lamina, but supports the reinforcing fibers. Example fibers include fiberglass, Kevlar, carbon, and graphite, while example matrix materials include thermosetting resins, polyester resins, and epoxies. Figure 1 shows an example composite cross section, with the fibers and resin identified.

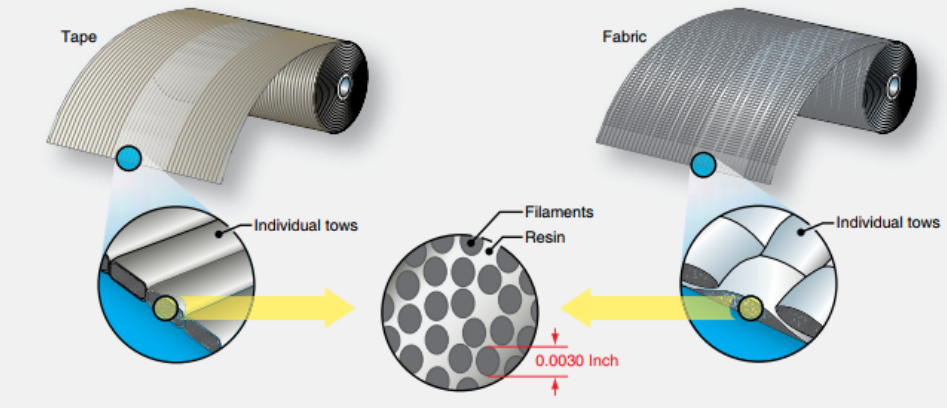

Figure 1: Example Composite with a Fiber Reinforced Resin Matrix (FAA, 2012)

1.1 - Motivation

Federal regulation requires an engine must be able to contain a blade and debris in the event of an engine blade out failure, in order to be certified for use. An engine blade out failure occurs when a fan or compressor blade becomes detached from the rotor. If the engine case is unable to contain the blade and debris, fuel takes, wings, or the fuselage can become penetrated by the blade, leading to catastrophic failure of the aircraft. As stated by Federal Aviation Administration (FAA) Regulation, part 33, section 94: *Blade containment and rotor unbalance tests,* it must be demonstrated by engine tests that the engine is capable of containing damage from a compressor or fan blade operating at maximum rotations per minute (FAA, 2017). While a blade out test can lead to certification of an aircraft engine, these tests are extremely costly and very little experimental data can be gained on the dynamics of the system. It is difficult to observe the dynamics of the system due to the engine components being destroyed by the high-speed fan blade and the subsequent debris during the testing. Figure 2 shows the resulting damage from two separate uncontained engine failures.

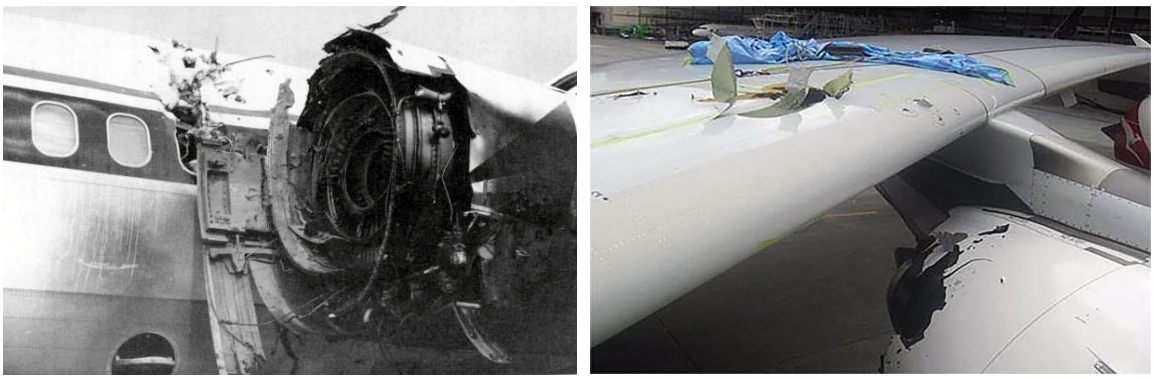

Figure 2: Uncontained Engine Failures, (Left) Delta Airlines Flight 1288 compressor rotor failure and fuselage damage (Right) Qantas Airlines Flight 32 turbine disk failure and wing damage (Bold Method, 2016)

Accurate computational models can be used to simulate blade out testing, as an alternative to the destruction of a fully manufactured engine. Simulations allow researchers to observe the dynamics of a blade out test, as well as verify various failure mechanisms without actually conducting blade out tests. While a failed blade out test would identify a single failure mechanism, and lead to a second blade out test to correct for this problem, an accurate model can easily be changed to accommodate various blade speeds, materials, and geometries without needing to rerun the entire simulation. While computational models cannot be used to completely replace the blade out tests, what is occurring in the system can be easily observed and necessary design changes can be identified without engine destruction. When the engine design process becomes iterative due to failures, accurate computational models can drive down the cost of development significantly.

1.2 - Focus and Objectives

Development of accurate computational models for composites requires understanding of the materials from which the composite is composed. Although all materials comprising a composite add to the overall strength, the matrix material's

properties become a significant factor when considering a blade out scenario, where there is predominantly transverse force applied to the composite (Littell, 2008). When conducting computer simulations using a micromechanics approach, experimental tensile, compressive, and shear data are needed for constitutive modeling of the resin matrix material (Littell et al, 2008). This research will be focused on obtaining the tensile test data to determine strain rate dependence and thermomechanical response of the composite matrix material, epoxy resin PR-520. This data will be used in conjunction with compressive and shear data to formulate an accurate computational model of a composite with PR-520 as the matrix material.

With the need for the matrix properties, there are two main objectives of this research:

1 - Capture full-field strain and full-field temperature data using Digital Image Correlation (DIC) and a high speed Infrared camera during tensile tests at strain rates of $0.01s^{-1}$, $1.0s^{-1}$, and $350s^{-1}$.

2 - Overlay IR data on DIC data to determine correlation between strain and temperature.

1.3 - Literature Review

The current research will build off of the previous techniques and experiments presented in the current chapter, providing background on the topic, applicability of previous techniques to epoxy resin testing, and how this research will serve as an extension of previous work. First, previous work highlighting the importance of thermomechanical coupling will be addressed. Next, the applicable methodologies for obtaining the desired data will be outlined, as well as the previous experiments where

these techniques have been employed. Finally, it will be highlighted how this work progresses from previous research.

When materials deform, there is a corresponding temperature change related to the deformation. For polymers, temperature changes include cooling during elastic deformation, and heating during plastic deformation. For most materials the plastic heating is more significant than elastic cooling and the temperature rise increases with increasing strain rate because there is less time for heat dissipation during the test. At high enough strain rates the tests can become nearly adiabatic with almost all heat generated, contributing to a temperature rise of the material. An increased temperature can affect the response of the material and the plastic deformation that is occurring (Seidt et al, 2017). For materials with low melting points, such as epoxy resins, even small temperature rises can prove significant to deformation and failure.

To be able to predict temperature fields and associated thermal softening, one must understand the coupling between the plastic deformation and the heat generation (Hodowany et al, 2000). Therefore, in order to produce an accurate computational model of a material it is important to know the Taylor-Quinney coefficient; the fraction, denoted as β, of plastic work converted to heat (Rosakis et al, 2000). The fraction β is the coupling factor between the mechanical and thermal response of a material and allows for the prediction of temperature rise for various loading conditions in a computational model. A single adiabatic experimental record of stress and temperature change, along with other known material characteristics, can lead to the determination of β (Rosakis et al, 2000).

Previous experiments have taken β as a constant for all materials and over all

strain rates as somewhere between 0.8 and unity; (Clifton et al, 1984) however, it has been shown that β is in fact a rate dependent, material specific variable (Rosakis et al, 2000). While more recent work has focused on the rate dependence of β for various materials (Seidt et al, 2017; for stainless steel, Kapoor and Nemat-Nasser, 1998; for titanium), little work has been done to determine the Taylor-Quinney coefficient and its rate dependence for polymers, and more specifically, epoxy resins.

Since it is now known that β can vary with strain rate, it becomes beneficial to conduct a series of varying strain rate tests. There are several techniques that can be used during these tests to obtain simultaneous full-field strain and temperature data. These methods can be separated into two distinct categories; contacting measurement devices such as thermocouples and strain gages, and non-contacting optical measurement devices such as cameras and infrared sensors. Recently, non-contact methods have become the preferred method because of the capability to measure data without affecting the response of the material from the fixing of sensors to the specimen. Optical techniques also have the capability to record data at much higher rates; limited only by the capabilities of the camera, making them ideal for short time scale, high strain rate tests (Seidt et al, 2017).

Non-contact optical techniques for displacement measurements that have been applied in previous research include interferometry methods (Post and Wood, 1989), video extensometers (Völkl and Fischer, 2004), laser speckle correlation (Anwander et al, 2000), and digital image correlation (DIC) (Lyons and Liu, 1996). Video and laser speckle correlation only provide area averaged measurements. These methods are not beneficial when the full-field displacements and strains are desired, as is the case with the current research. Digital image correlation is capable of determining all three

displacement components simultaneously with nothing more than a calibrated pair of cameras (Cholewa et al, 2016). Digital Image Correlation is relatively easy to implement and with various post processing software available, has become a preferred method of determining full-field deformation.

Fewer non-contact temperature measurement techniques have been applied but include infrared pyrometers (Summers et al, 2014.), infrared thermography (Summers et al, 2014, Seidt et al, 2017), and temperature calibrated cameras (Ortreu et al, 2008). Infrared pyrometers are point measurement devices and do not lend themselves to useful application when full-field temperature measurements are desired. Using temperature calibrated cameras allows for simultaneous measurement of full-field strain and temperature at a single location on the specimen using only one camera for 2-D DIC or a stereo pair of cameras for 3-D DIC. While this method simplifies testing and post processing, the cameras in the study were not calibrated for surface emissivity and work must be conducted to determine a method for measuring true temperatures (Ortreu et al, 2008). Infrared thermography can be conducted with a single infrared camera, the parameters of which are determined from the testing speed (Seidt et al, 2017). If the specimen is assumed to be sufficiently thin so that temperature gradients can be neglected, IR images can be captured on the back side of the specimen relative to the visible cameras used for DIC images. The use of the IR camera allows for customization of exposure time, frame rate, and resolution, independent of the parameters the visible cameras are operating at, but these methods require a transformation between the temperature and strain coordinate systems following data acquisition (Cholewa et al, 2016).

The range of desired strain rates for the testing requires the use of two distinct testing apparatus; a servo-hydraulic load frame, and a direct tension Split-Hopkinson bar. The servo-hydraulic load frame is pictured in Figure 3.

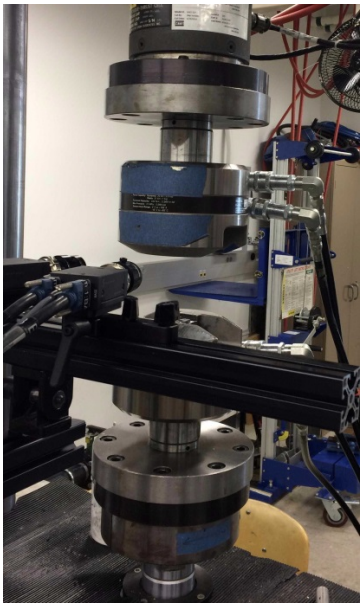

Figure 3: Servo-Hydraulic Load Frame

The servo-hydraulic load frame is accurate for low strain rates, up to about $1.0s^{-1}$, where the forces can be measured directly by a load cell. For higher strain rates, on the order of $400s^{-1}$ to $5000s^{-1}$, the Split-Hopkinson bar must be used (Seidt et al, 2017). In a Split-Hopkinson bar experiment, a specimen is placed between two bars, and the specimen is loaded by a wave generated in the end of the incident bar. During loading of the specimen, a portion of the wave is reflected back to the incident bar, and the remainder of the wave passes through the specimen into the transmitter bar. The amplitude of the generated wave is designed so that the incident and transmitter bar remain elastic while the specimen is loaded beyond its elastic limit. Knowing the wave amplitude, specimen and bar dimensions, and using elastic wave theory, the force in the

specimen as well as the strain and strain rate can be calculated (Gilat et al, 2009). A schematic of a Split-Hopkinson bar can be viewed in Figure 4.

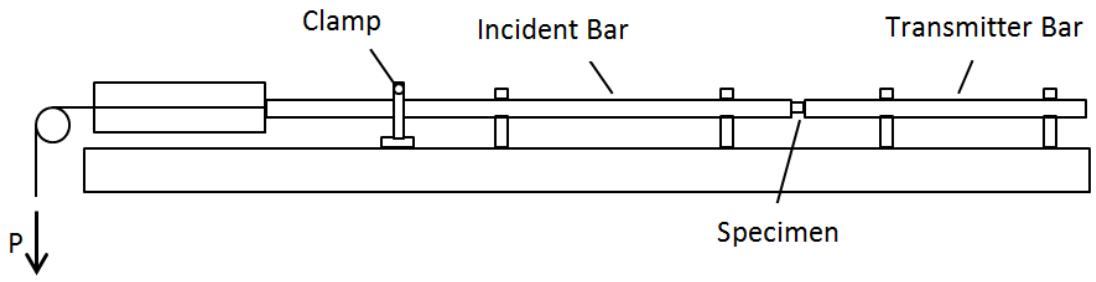

Figure 4: Split-Hopkinson Bar Schematic

While there have been no attempts to capture the thermomechanical response of Epoxy Resin PR-520, there is previous research looking into the mechanical properties of PR-520 that this research will be building off of. Previous testing of the epoxy resin PR-520 included tension and torsion tests conducted at 5E-5s^{-1}, 2s^{-1}, and 400-700s^{-1}. From the tensile stress-strain curves it was observed that the maximum stress for the intermediate and high strain rates was approximately the same and higher than the maximum stresses in the low rate tests. The testing also showed that as the testing rate was increased, PR-520 acted as a more brittle material and that the response of PR-520 is sensitive to the strain rate at which the test is occurring (Gilat et al, 2007). While this research highlights trends to look for in the current research, the testing was conducted using conventional strain gages, and no DIC. The problem with this is that in higher rate Split-Hopkinson bar experiments, if significant deformation occurs outside the gage section, or during necking, the strains calculated from wave theory are no longer valid. However, digital image correlation can provide accurate full field strain even when necking occurs (Gilat et al, 2009).

These tests were also conducted using different specimen geometry than what is used for the current research. Due to the difficulty with producing large resin specimens that conform to ASTM D-638, custom smaller geometries have been chosen. The specimens were designed to be cylindrical with a gage length of 0.125", a gage diameter of 0.125", 1" ends for gripping, and a large transition radii between the end and the gage. These specimens were small enough that many could be obtained from a single resin sheet, and the geometry still allows for a uniform stress state in the gage section. The design of the specimen was intended to allow for later Split-Hopkinson bar tests with the same geometry (Littell, 2008).

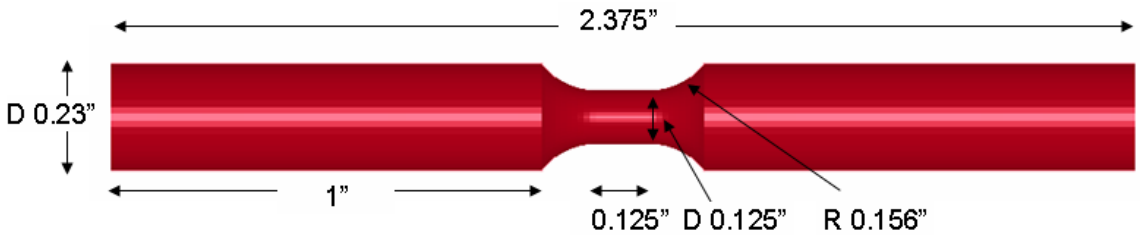

Figure 5: Specimen Geometry (Littell, 2008)

The proposed geometry has been used for tests with epoxy resin Epon E862. Tensile testing was conducted at 1E-5s^{-1}, 1E-3s^{-1}, and 1E-1s^{-1}. While these low rate tests did not confirm the applicability of the geometry for use in Split-Hopkinson bar tests, it was stated that the technique and specimen geometry can easily be applied to other types of resins. It was also stated that the results obtained from this testing can easily be used to develop the constitutive model of the resin for use in commercial finite-element codes (Littell et al, 2008)

1.4 - Significance

Although the material for this research has been examined in previous work (Gilat

et al, 2007), and the techniques that will be applied for this research have been applied to stainless steel (Seidt et al, 2017), this will be the first attempt to capture the simultaneous full-field temperature and deformation for epoxy resin PR-520. The data that will be obtained from these tensile tests will allow for corrections to the constitutive model for PR-520 by allowing for an accurate thermomechanical response to be identified. Ultimately, the data obtained in this research will lead to more accurate computational models for composites in impact loading situations.

1.5 - Overview

This thesis has three remaining chapters. Chapter 2 outlines the methodology for conducting this research. A detailed discussion of the emissivity calibration, specimen preparation, the setup for the three different speed tests, and the technique for overlaying the infrared and deformation data on a single image will be the focus of this chapter. Chapter 3 lays out the results from the testing at the three different strain rates, and discusses these results and their comparison along with any shortcomings with the current research and potential improvements for future work on this topic. Chapter 4 serves as a conclusion to this thesis and highlights how this research contributes to other current works, the direction of future work resulting from this research, and where these techniques can be applied to other works.

CHAPTER 2: METHODOLOGY

To obtain the desired data, two optical techniques were used to capture the full-field deformation and full-field thermal response of the specimens; Digital image correlation, and high speed infrared thermography. 3-D DIC uses a pair of cameras that can be calibrated to provide a synchronized 3-D view of the specimen. 2-D DIC is used for the high rate test because the necessary frame rates to capture the deformation were high enough that any of the pairs of cameras available were unable to capture the deformation. Proper preparation of the specimen surface with a stochastic speckle pattern allowed the commercial software Vic-3D and Vic-2D to track the relative displacement of points on the specimen surface, and use these tracked deformations to determine strains. For infrared thermography, a high speed infrared camera was used to capture the temperature of the viewing surface. The main concern with infrared thermography is the calibration of the camera for the surface emissivity, which often is unknown. The infrared camera used for the current work assumes the surface emissivity is unity, and the determination of the emissivity and correct calibration are crucial to obtaining accurate data. While emissivity values can often be found in literature, the true emissivity depends on many factors, and a calibration using real samples is the only way to obtain reliable, test specific emissivity values (Seidt et al, 2017).

A servo-hydraulic load frame is suitable for the tension tests with strain rates of $0.01s^{-1}$ and $1.0s^{-1}$, and the direct tension Split-Hopkinson bar is suitable for the $350s^{-1}$ tests. The material is relatively brittle when compared to metals, and because of this it was determined that adapters should be machined so that the specimen was not directly gripped by the hydraulic grips of the load frame in order to prevent crushing the ends of

the specimen, or supplying enough shear force to break the specimens during loading due to grip misalignment. Adapters also needed to be machined for the Split-Hopkinson bar tests, because there is no gripping mechanism involved. For these tests the specimens were fixed to adapters, the ends of which were then glued to the ends of the transmitter and incident bars.

The testing that was conducted is outlined in Table 1. Three tests each at $0.01s^{-1}$, $1.0s^{-1}$, and $350s^{-1}$. Infrared data was recorded for each test using the Telops Fast IR infrared camera. DIC data was captured using the FastCam MC2's for the $0.01s^{-1}$ and $1.0s^{-1}$ tests, and the Shimadzu HPV-X2 High-Speed Video Camera for the $350s^{-1}$ tests. The Telops Fast IR infrared camera can record 2000 fps in full resolution and up to 90,000 frames per second, at a reduced resolution. The MC2 cameras are capable of recording up to 8000 frames per second, and the Shimadzu cameras can record up to 10,000,000 frames per second at reduced resolutions.

Table 1: Test Matrix

PR-520 Epoxy Resin Tensile Test Matrix									
Material	Strain Rate	Test Name	Date	Test Success	Trigger Data	DIC Inspection	DIC/MTS/Wave Sync	Max Temp. Data	Align
PR-520 Epoxy Resin	1s-1	PR520-Tension-N1	6/27/2017	Y	Y	Y	Y	Y	Y
	1s-1	PR520-Tension-N2	6/29/2017	Test Complete	Y	Y	Y	Y	Y
	1s-1	PR520-Tension-N3	8/14/2017	No Trigger					
	1s-1	PR520-Tension-N4	8/14/2017	Y	Y	Y	Y	Y	Y
	1s-1	PR520-Tension-N5	8/14/2017	No IR					
	1s-1	PR520-Tension-N6	8/15/2017	Y	Y	Y	Y	Y	PR520-1s-1-N4_Align
	0.01s-1	PR520-Tension-N1	8/22/2017	Y	Y	Y	Y	Y	Y
	0.01s-1	PR520-Tension-N2	8/22/2017	No Trigger					
	0.01s-1	PR520-Tension-N3	8/24/2017	No Trigger					
	0.01s-1	PR520-Tension-N4	8/24/2017	Y	Y	Y	Y	Y	Y
	0.01s-1	PR520-Tension-N5	8/25/2017	Y	Y	Y	Y	Y	Y
	350s-1	PR520-Tension-N1	1/25/2018	Glue Failure					
	350s-1	PR520-Tension-N2	1/26/2018	Flange Shear					
	350s-1	PR520-Tension-N3	1/29/2018	Glue Failure	Y	Y	Y	Y	Y
	350s-1	PR520-Tension-N4	1/30/2018	Test Complete	Y	Y	Y	Y	Y
	350s-1	PR520-Tension-N5	2/25/2018	Bad Waves					
	350s-1	PR520-Tension-N6	2/27/2018	Bad Waves					
	350s-1	PR520-Tension-N7	3/1/2018	Y	Y	Y	Y	Y	Y
	350s-1	PR520-Tension-N8	3/2/2018	Y	Y	Y	Y	Y	Y

2.1 - Emissivity Determination

As was previously discussed, emissivity determination of the material is one of the most important requirements to obtain correct temperature readings. Using the Telops Fast IR high-speed infrared camera, recording in in-band radiance, the radiometric temperature can be determined if the emissivity of the specimen, as well as the surrounding radiance are known. Due to the fact that the IR camera assumes an emissivity of unity, any temperature reading by the camera is effectively assuming all temperature is emitted by the surface being viewed. In reality this is not the case because there are no ideal black body materials in existence. This means that a portion of the temperature reading from the surface of a specimen is actually the reflected irradiance from the surroundings. By recording in in-band radiance, the surrounding radiance could be measured, and this allowed for the calculation of true in-band radiance and true temperature.

In order to determine the surrounding radiance, measurements were taken viewing a piece of aluminum foil with the IR camera. The emissivity of the aluminum foil is approximately 0.04, and it was then assumed that all radiance the camera viewed on the foil is reflected radiance from the surroundings. The foil was crumpled so that the camera was not viewing the reflection of a surrounding object. If this occurred, the surrounding radiance value would be the radiance of the object that was being reflected rather than the surroundings. The surrounding radiance in the environment testing was conducted in was typically between 1.65 and 1.75 photons s^{-1} m^{-2} sr^{-1}, but it was necessary to get a surrounding radiance measurement anytime testing conditions changed. The foil panel used can be viewed in Figure 6.

Figure 6: Aluminum Foil for Surrounding Radiance Calculation

The true radiance of the specimen could be found using the following equation.

$$\mathrm{Ltarg} = \frac{\mathrm{Ltot} - \mathrm{Lsurr}}{e} - \mathrm{Lsurr} \qquad (1)$$

Where *Ltarg* is the true radiance from the specimen, *Ltot* is the radiance measured off the specimen by the IR camera, *Lsurr* is the surrounding radiance, and *e* is the emissivity value. Using equation (1), and a measured surrounding radiance, the true radiance from the specimen could be calculated. To convert the IR reading from photons s^{-1} m^{-2} sr^{-1} to radiometric temperature, equation (2) must be solved for various temperatures and wavelengths.

$$L_\lambda = \frac{2E24*h*c^2}{\lambda^5} * \frac{\frac{1}{e^{1E6*h*c}}}{(\lambda*k*T)-1} \qquad (2)$$

Equation (2) is used to find the spectral radiance per μm for a black body where *h* is Planck's constant, *c* is the speed of light, and *k* is Boltzmann's constant. Here *T* is an arbitrary temperature, and λ is an array of values for wavelength, which for the Telops Fast IR camera is between 3 and 5 μm. Spectral radiance is then found for the temperature at every λ value in the array. For a given temperature, all spectral radiance

values can be integrated over the wavelength interval to find the in-band radiance of a black body, and the process can be completed for all temperatures seen in any test. Using an array of temperatures, an array of black body, in-band radiances can be determined that correspond to the temperature array used. Interpolating between the in-band radiance and temperature using the true in-band radiance of the specimen, allowed for the true temperature of the specimen to be found.

To determine the emissivity of the specimen, an OMEGA precision fine wire thermocouple was attached to a specimen that had already been tested. The camera was aimed at the broken specimen with the thermocouple, and set to a recording frequency matching the Omega HH309A data recorder. The specimen was then heated to an arbitrary temperature that was higher than what was expected during testing. Once the specimen had been heated, the data logger and camera were set to begin recording the radiometric temperature for the thermocouple and in-band radiance for the IR camera. For the emissivity determination, both were set to a frequency of 1 Hz, and recording occurred as the specimen cooled for approximately 150 seconds. Using equations (1) and (2), the emissivity was adjusted, and temperature calculated, until the curve for the temperature seen by the IR camera matched the curve of the temperature recorded by the thermocouple and data logger. Figure 7 shows a broken specimen with the thermocouple attached to the surface, and Figure 8 shows the temperature curves obtained from the thermocouple and the IR camera.

Figure 7: Specimen with Thermocouple

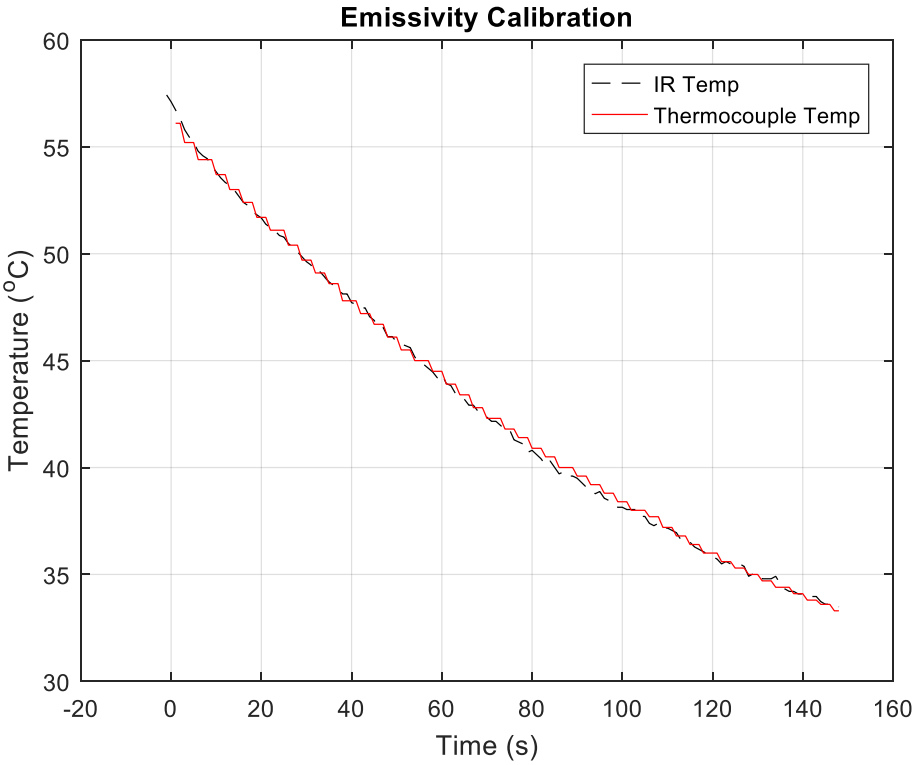

Figure 8: Emissivity Calibration Curves

From the emissivity calibration, it was determined that the emissivity of the material was equal to 0.83, which was a sufficient enough value to not require any special specimen

preparation for viewing by the IR camera. The equations presented in this section as well as the procedure to determine surrounding radiance are also applied to convert from in-band radiance to radiometric temperature after each test.

2.2 – Specimen Preparation

The as received specimens were a flat black color, and as was noted in the previous section, the emissivity was found to be high enough that no special specimen preparation was required for viewing by the infrared camera. Figure 9 shows the appearance of an unaltered specimen.

Figure 9: As Received Specimen

In order for DIC to track relative motion of points on the specimen there must be a random contrast applied that allows the software to determine when certain points of the specimen move through groups of pixels. A calibration of the stereo pair of cameras using a glass panel calibration grid, moved about the three principle axis, allows for calculations of the mm per pixel in a series of successive images. For 2-D DIC, a single

image is required to calibrate the mm per pixel in the axial direction of the test. Knowing the mm per pixel for any given test allows the software to correct from pixels of displacement to mm.

To apply the stochastic speckle pattern for DIC tracking, the specimens were first taped to protect the side that would be viewed by the infrared camera. The uncovered side of the specimen was then sprayed with a layer of Rust-oleom Ultracover flat white primer. A light speckling of Rust-oleum Ultracover flat black primer was then applied to the white part of the specimen, in order to achieve the best contrast possible. A speckled specimen can be viewed in Figure 10.

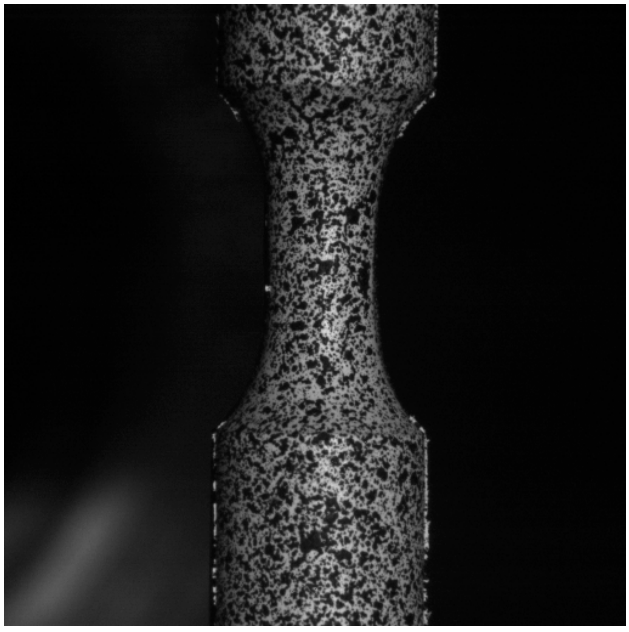

Figure 10: Applied Speckle Pattern

A properly speckled specimen allowed for data collection at all points of the specimen within the view of the cameras.

For all tests, due to the low exposer times of the DIC cameras, it was necessary to have a light source illuminate the side of the specimen that was being viewed by the DIC

cameras. For these tests it was determined that a Visual Instrumental Corporation LED light source would be used because it could supply sufficient light for the DIC cameras, while operating at wavelengths that would not be visible to the infrared camera. The Light Source can be seen highlighted in Figure 11, in place for a Split-Hopkinson Bar test.

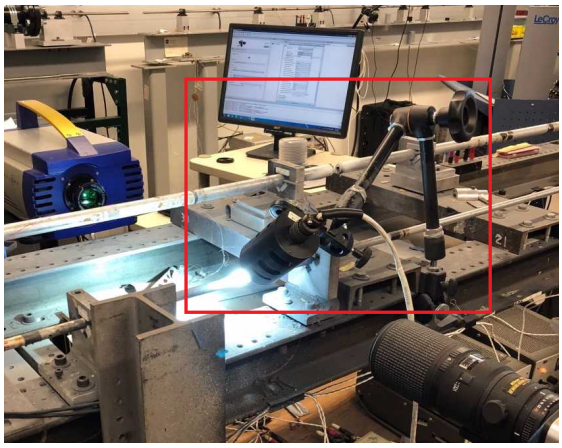

Figure 11: Light Source

It was discovered that the light source would heat specimens prior to and during testing. For the intermediate and low rate tests heating before the test was not a significant issue because the light could be turned on just before the test. However, in the low rate tests, the test duration was long enough that heating from the light source could be observed during testing. In the high rate tests the light contributed to heating before the test, because the light source needed to be turned on several moments prior to the testing. The effects of which could be viewed as high initial temperature readings on the specimen. It was determined that these high temperature readings were a result of the light heating the specimen because a Temperature vs. Time plot for a high rate test returns to room temperature after the specimen has failed and the IR camera is viewing the surrounding. A plot of the temperature vs. time can be seen in Figure 12.

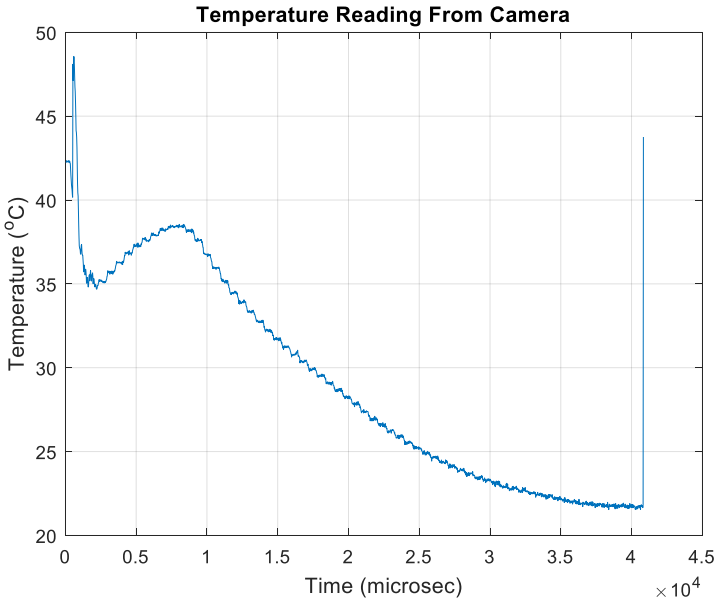

Figure 12: Temperature vs. Time

2.3 - 0.01s^{-1} Test Setup

As was previously stated, it was determined that a bi-axial servo-hydraulic load frame would be suitable for the 0.01s^{-1} strain rate tests. The load frame is controlled by the MTS station manager software. The use of the bi-axial load frame allowed for the programming of the actuator to ensure that no torque was applied to the specimen during pure tension tests. To achieve this, a short steel bar was gripped by both the top and bottom hydraulic grips. The torque was then set to zero, which would result in the bottom actuator head rotating to adjust the angle between the top and bottom heads, until zero torque on the bar was achieved. Once the torque reading was zero, the angle was set to remain constant to the angle that resulted in zero torque. This made it possible for a load to be applied in the uniaxial direction of the specimen without resulting in a torque on the specimen.

In metal tension tests on the hydraulic load frame the hydraulic grips of the machine can be used to directly grip the tabs of the specimen without supplying a significant initial force to the specimen. Once the specimen is firmly gripped and the desired grip pressure was reached, the load frame would zero itself so no initial load was applied to the specimen. For the specific material and geometries used for the current tests, there was concern over whether or not this initial force during the gripping procedure would be significant enough to negatively affect the specimens. It was determined that a double jointed universal joint could be used to relieve the compressive force put on the specimen during the gripping procedure. To ensure this, the universal joint was gripped directly by the top hydraulic head of the frame using a 0.79”-1.07” serrated vee wedge grip to a pressure of 1500 psi, to ensure no slipping at the grip. The specimen was then pinned to the universal joint so that it would hang down into the frame of view of the FastCam MC2 cameras and the Telops Fast IR camera. The bottom of the specimen could then be gripped directly by a 0.12”-0.37” serrated vee wedge grip on the bottom head of the frame. The double universal joint also acted to correct for any misalignment between the grips, to prevent a shear force being applied to the specimen during loading. Minor shear forces could lead to noticeable variations in the load-displacement curves for specimens with low failure strengths. The vee grips used are shown in Figure 13.

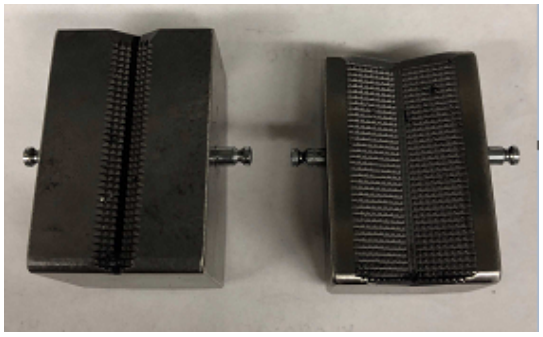

Figure 13: (Left) 0.12-0.37 vee grip (Right) 0.79-1.07 vee grip

As the bottom of the specimen was gripped and the upward force from the gripping was applied to the specimen, the universal joint would give at the two connections to dissipate the force away from the specimen. The pressure of the bottom grip was then increased to 400 psi to prevent slipping between the specimen and the grip during testing, but also low enough to avoid crushing the bottom tab of the specimen. An initial preload of three pounds was then applied to ensure all components were properly set before beginning a test. If the load frame were shut down between testing, the full procedure was repeated to ensure proper conditions during testing. Otherwise, the specimen was pinned to the universal joint and the gripping procedure for the bottom of the specimen was repeated.

To attach the specimens to the universal joint, adapters had to be machined that could be glued to the specimen, and then pinned to the universal joint. Figure 14 shows the adapters designed for the low and intermediate rate tests.

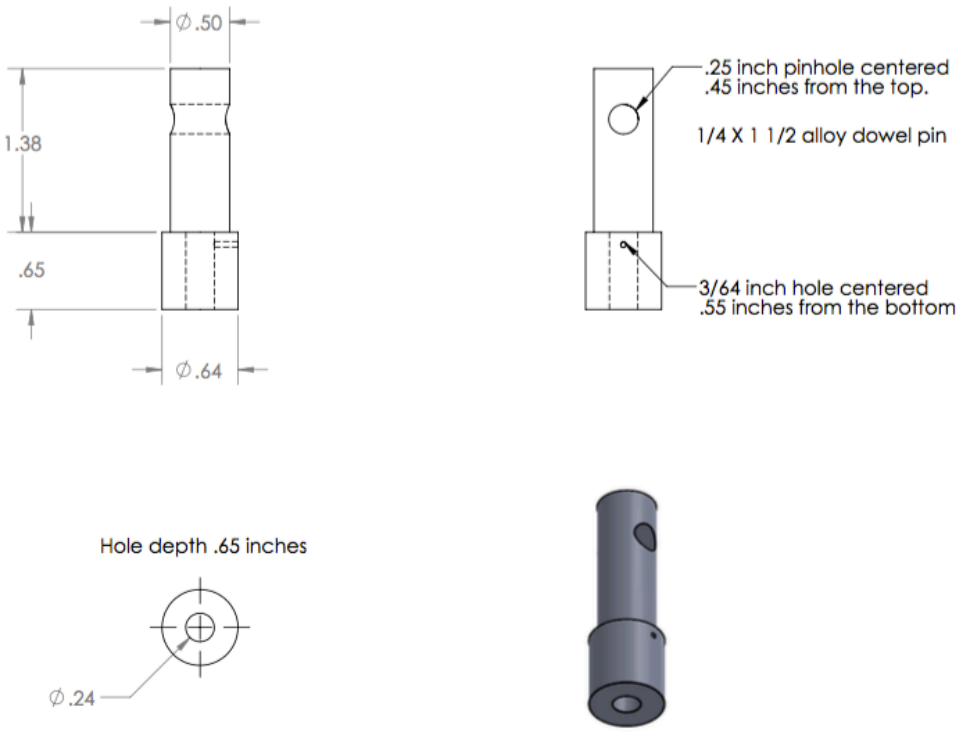

Figure 14: Low Rate Adapter

The depth of the uniaxial hole made it possible to insert the top end of the specimen, and there was 0.01" tolerance between the hole diameter and specimen diameter so that J-B weld two part epoxy and hardener could be used to hold the specimen in place. To ensure a good bond with the glue, both the specimen and adapter had their surfaces roughened with sand paper. These surfaces were cleaned with acetone, and prepared with a conditioner and a neutralizer. The epoxy was applied, and given at least 24 hours to cure before testing. The painting procedure for these specimens was completed after they were glued to an adapter and just before testing occurred. A broken, glued, pinned specimen can be viewed in Figure 15.

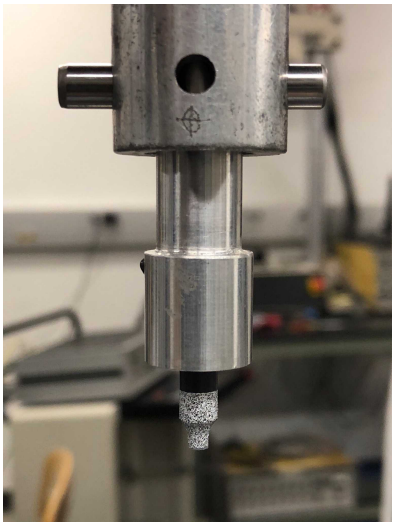

Figure 15: Glued, Pinned Specimen

To run the tests, the MTS program allowed a series of commands to be input that were timed and could run in succession to one another, as well as at the same time as one another. This made it possible to send a single pulse that triggered both sets of cameras to begin acquiring images, and for the software to begin recording data from the load cell. For these tests, both sets of cameras were run at the same frame rate of 50 frames per second (FPS). The lowest frame rate the MC2 cameras are designed to record at is 80 FPS and a waveform generator was used so that the cameras were triggered to record 1 out of every 5 images. The MC2 cameras were then run at 250 FPS only storing 50 FPS. An arbitrary time after data and images started being recorded, the actuator head was instructed to begin pulling the specimen at the desired rate. For the strain rate of $0.01s^{-1}$ this corresponded to pulling the full gage length (.125") in 100 seconds. The distance and duration of the test can be found using the equations for strain and strain rate.

$$\varepsilon_e = \frac{\Delta l}{l_g} \tag{3}$$

Where ε_e is strain, Δl is the change in gage length and l_g is the original gage length. t in equation (4) is time and $\dot{\varepsilon}$ is strain rate.

$$\dot{\varepsilon} = \varepsilon_e / t \quad (4)$$

The program then instructed the load frame to stop after 100 seconds and the cameras to stop acquiring data.

The cameras were placed on opposite sides of the test frame so that they were viewing opposite sides of the test specimen. Assuming that the temperature gradient is negligible within the specimen, the temperature data taken on the back side of the specimen could be superimposed over the deformation data gathered on the opposite side. Figure 16 shows the IR data taken on one side of the specimen on the left, with the original deformation data from the other side of the specimen on the right.

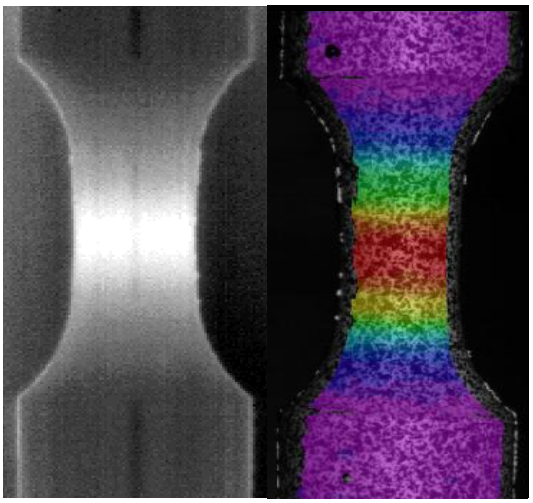

Figure 16: Simultaneous Image Acquisition (Left) Thermal (Right) DIC

The waveform generator also ensured that both camera sets were simultaneously triggered. Due to the low required frame rates of these tests, both the thermal and visible cameras acquired images at their full resolutions. With both cameras operating at the same speed only the time of acquisition of the first images was needed to line up the two data sets in time. The parameters used for the two camera sets can be viewed in Table 2.

Table 2: Camera Parameters for $0.01s^{-1}$ Tests

Camera	Strain Rate	Resolution	Frame Rate	Exposure Time
IR	1.00E-02	(256 x 256)	50	150 µs
MC2	1.00E-02	(512 x 512)	250	100 µs

The axial force and the displacement of the load frame were recorded in the MTS station manager, and this data was used to calculate strains and deformations. However, a virtual extensometer 3mm in length was also used along with failure point data to get a better representation of deformations within the gage section. A comparison of force-displacement curves using DIC and frame data for a $0.01s^{-1}$ test is shown in Figure 17.

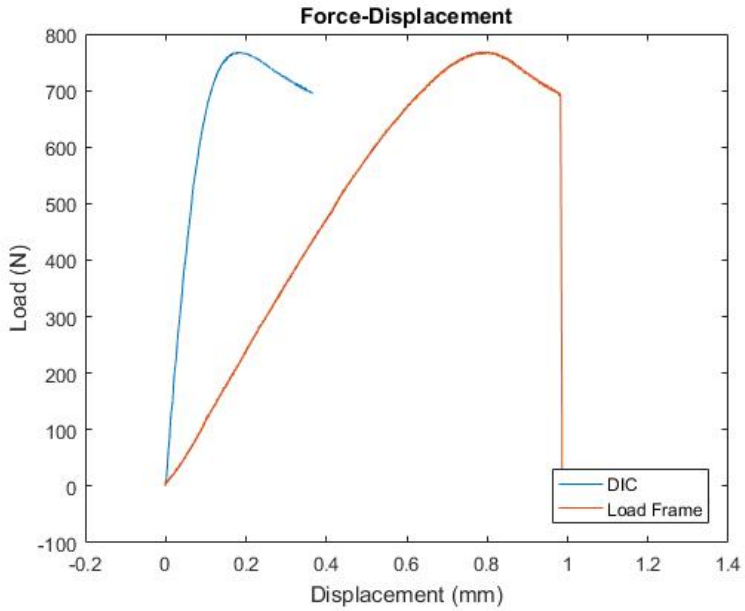

Figure 17: Comparison of Force-Displacement using Frame data and DIC

The reason for the large variance in deformation is due to the fact that the load frame records total deformation, which in this case, involves deformation in the flanges of the specimen, where the specimen is glued to the adapter, where the adapter is pinned to the universal joint, and deformation within the universal joint itself. DIC uses the virtual extensometer deformation data to calculate the deformation within the gage

section of the specimen, which is a better representation of deformation for calculating strain. Figure 18 shows a specimen with DIC data and a virtual extensometer.

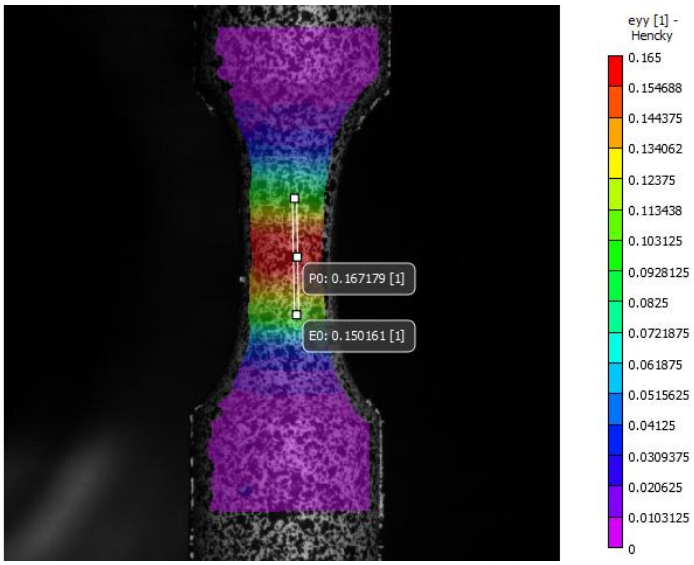

Figure 18: DIC with Extensometer and Failure Point

A pair of blackout curtains was draped over the testing apparatus to provide a constant surrounding for the tests. While these curtains did not block all surrounding radiance, they protected against changes in surrounding radiance that would occur from changes within the laboratory. Once the blackout curtains were in place, surrounding radiance measurements were taken as described in Section 2.1. The final test setup is seen in Figure 19.

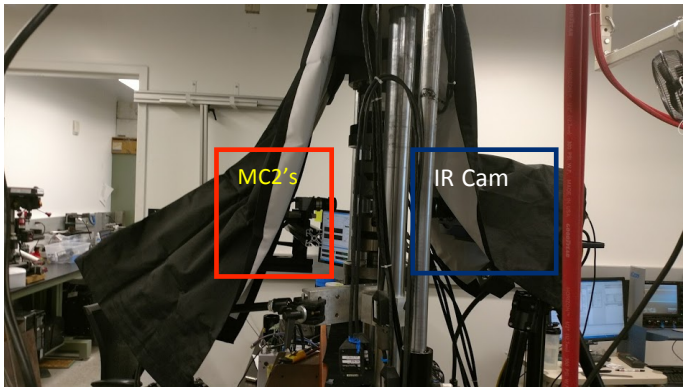

Figure 19: Test Setup with Blackout Curtains

2.4 – 1.0s^{-1} Test Setup

The test setup for the 1.0s^{-1} tests mirrored the setup from the 0.01s^{-1}, aside from the pull rate of the load frame and the camera parameters. To achieve the desired strain rates the actuator pulled the specimen one full gage length in 1 second. For the initial test at this rate, the FPS of the cameras were matched at 2000, and this was still low enough that full resolution could be used for both the DIC and infrared cameras. However, it was determined that faster frame rates would allow for better data acquisition and the rates were doubled to 4000 FPS for each camera set. In order to achieve higher frame rates the resolutions had to be narrowed and these parameters can be seen in Table 3.

Table 3: Camera Parameters for 1.0s^{-1} Tests

Camera	Strain Rate	Resolution	Frame Rate	Exposure Time
IR	1	(256 x 256)	2000	50 µs
		(128 x 256)	4000	35 µs
MC2	1	(512 x 512)	2000	156 µs
		(512 x 256)	4000	100 µs

Narrowing the windows for the cameras had no negative impacts on the data acquisition because the gage section of the specimens was small enough that the cameras could still capture full-field data at the reduced resolutions. The same adapters as were used for the 0.01s^{-1} along with the same universal joint were once again utilized for these tests. It was determined that the J-B Weld two part epoxy would be able to sustain the loads that would be seen during testing. During testing it was determined that if the pressure of the hydraulic grip on the bottom of the specimen was 600 psi or more, it would cause a failure in the flange of the specimen during testing. The initial pressure used was 600 psi, but it was found that 400 psi was sufficient to hold the specimens at this strain rate and loading.

2.5 – 350s^{-1} Test Setup

To achieve strain rates of 350s^{-1} the Direct Tension Split-Hopkinson bar was required. The ends of the Split-Hopkinson bar have no mechanism for gripping specimens, and adapters were required to glue the specimen to the ends of the bars. The adapters were designed so that their outer diameter matched the diameter of the Split-Hopkinson bar. The material chosen for the adapters was 6061 aluminum so that the properties would match those of the bar and not cause any impedance. Figure 20 shows the adapters used for the high rate tests. The diameter of the uniaxial hole had a tolerance of 0.01" in order to glue the specimen to the adapter similar to the low and intermediate rate tests.

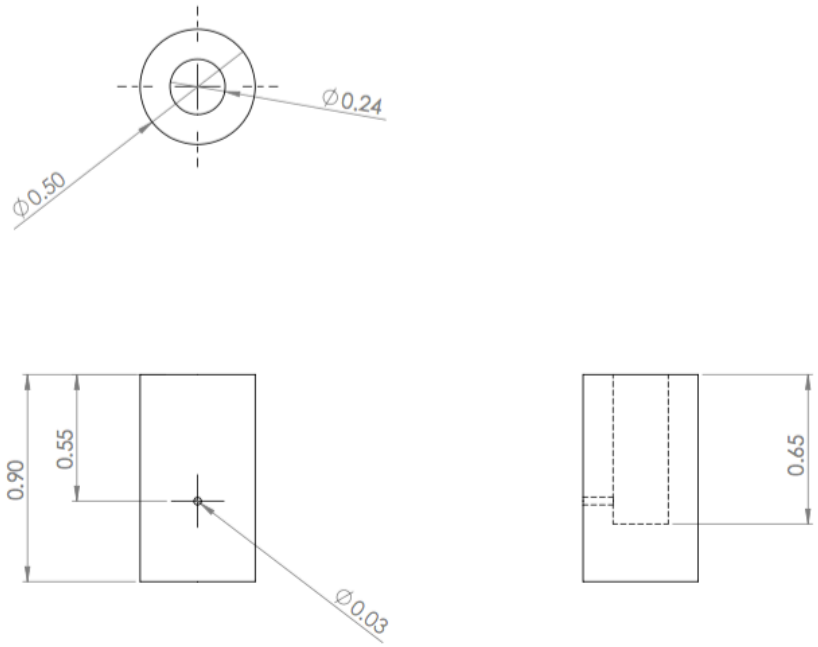

Figure 20: High Rate Adapters

To prepare the specimen for attachment to the bar the same procedure was repeated that was used in the low and intermediate rate tests. However, the flat bottoms of the adapters, as well as the bar, were roughened with sand paper before being cleaned with acetone and prepared with conditioner and neutralizer. Preliminary tests showed that

the J-B Weld epoxy could not withstand the forces present in these tests, and the glue used to hold the adapter to the bar, and the specimens to the adapters, was changed to Loctite Ablestik 2106T Bipax. There were also issues with the specimens shearing in the flange section within the adapter. It was determined that this issue could be addressed by shortening the grip section of the specimen by ~0.25 inches on each end to mitigate any initial misalignment. The specimens were then glued to the adapters the same way as the previous tests. A shortened specimen can be seen on the left of Figure 21 with an as received specimen on the right.

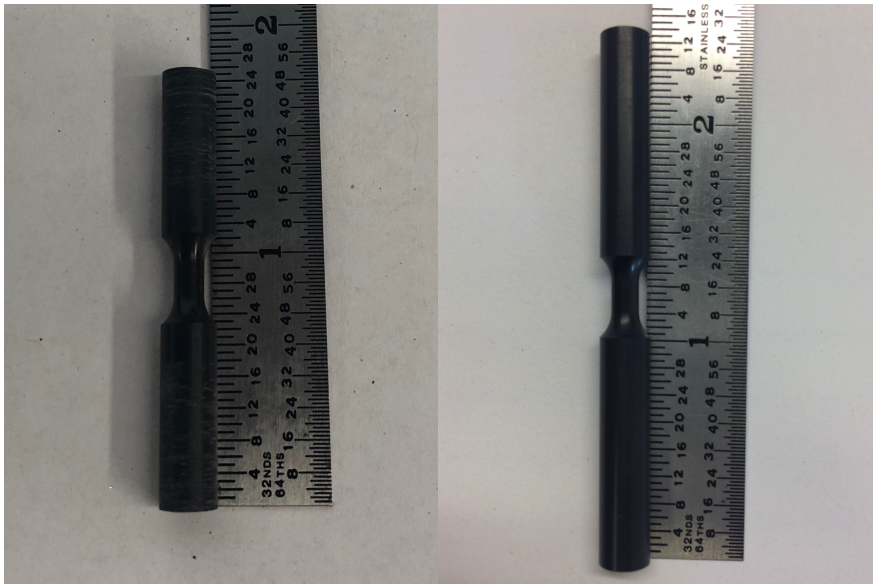

Figure 21: Specimen Size Comparison

Due to the short duration of the tests, it was necessary to run the cameras at significantly higher frame rates than the low and intermediate rate tests. Due to the necessary frame rates exceeding the capabilities of the FastCam MC2's, the Shimadzu HPV-X2 high speed camera was chosen for DIC, but synchronizing two Shimadzu HPV-X2's has not been achieved and it was determined that 2-D DIC would be acceptable for these tests. The high-speed capabilities of the Shimadzu HPV-X2 made it possible to

record at full resolution for these tests. The infrared camera was run at the highest possible speed that still allowed for the capture of full-field data on the specimen. When a strain gage on the incident bar detected the wave, both cameras were triggered by a waveform generator. The camera parameters used for these tests can be viewed in Table 4.

Table 4: Camera Parameters for $350s^{-1}$ Tests

Camera	Strain Rate	Resolution	Frame Rate	Exposer Time
IR	350	(64 x 20)	44,000	10μs
HPV-X2	350	(400 x 250)	500,000 400,000	500ns

While wave theory and the resulting data from the strain gages on the incident and transmitter bar are beneficial for finding the loading on the specimen, it has been shown that the displacement calculations from the wave data is not always accurate. Similar to the errors with the MTS frame, finding strains with wave theory finds all deformations in a test including deformations within the gage section. The strain gages on the bar are sensitive to deformations in the glue holding the specimen to the adapter, the glue holding the adapter to the bar, and deformation within the flanges of the specimen. The variance in the Load-Displacement curves for a single test at $350s^{-1}$ can be seen in Figure 22, and the pattern closely resembles the results from the lower rate tests on the MTS frame. Specifically, larger deformations are detected using the data from the load frame and wave theory.

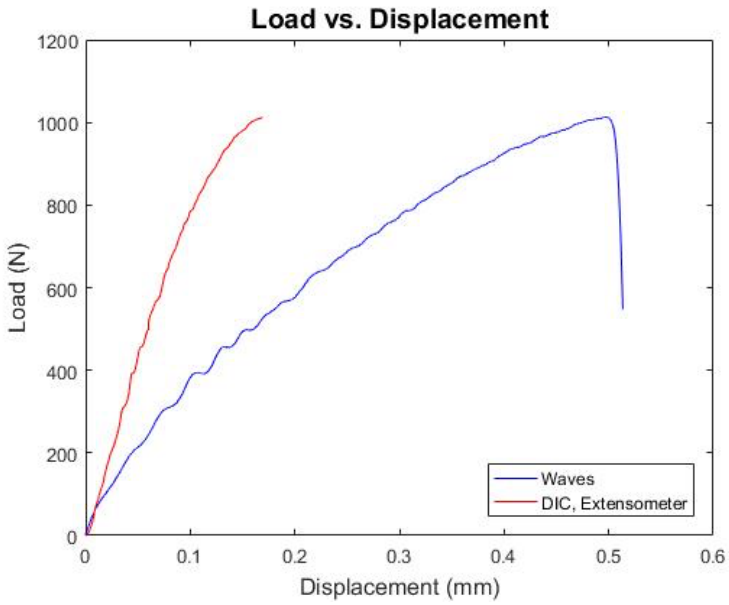

Figure 22: Comparison of Force-Displacement using Strain Gage Data and DIC

The Shimadzu and IR cameras were set up on opposite sides of the test apparatus, and the assumption was made that temperatures seen on one side of the specimen could be considered uniform throughout the specimen. The test setup was covered with blackout curtains and surrounding emissivity measurements were taken at the conditions at which testing occurred. The high rate test setup is pictured in Figure 23.

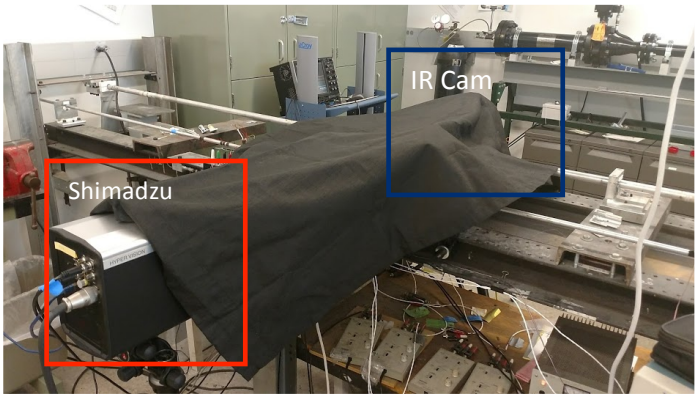

Figure 23: 350s^{-1} Test Setup

2.6 – Image Alignment

Once DIC and thermal images had been acquired, it was necessary to overlay the data sets so thermal data could be correlated to any DIC data point. Due to the fact that the resolutions of the cameras did not always match, the thermal images needed to be expanded as well as flipped to match the axis of the DIC image. DIC tracks movements of points while the infrared camera only records pixel values. By overlaying the two data sets it was possible to find temperature values at points rather than pixels.

In order to overlay the data sets, it was important to capture calibration images, using the same glass calibration grid that was used for the 3-D DIC calibrations for the low and intermediate rate tests; before the cameras were moved from the locations used for testing. The calibration panel was either held in the grips where the specimen was during the test, or in the case of the high rate tests, the grid was held where the specimen previously was using a C-clamp. Images were taken with the DIC cameras and the IR camera with either a light source or a heat source behind the grid to illuminate the circles. The resulting images can be seen in Figure 24.

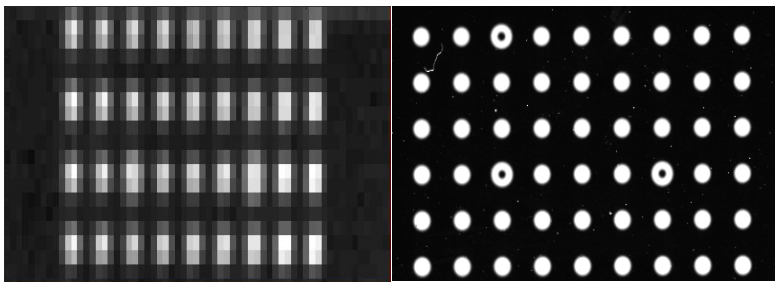

Figure 24: (Left) IR Calibration Image, (Right) DIC Calibration Image

Once both images had been acquired, MATLAB was used to transform the IR image in the three principle directions, and in pixel count. To overlay the IR image onto the DIC image the *x* coordinates of the IR image needed to be flipped using the function

flip. The centers of the circles were then identified, and ordered so that each circle in the IR image matched with a circle in the DIC image. Due to the fact that the resolution of the IR image was often smaller than the DIC image, it was important to make sure that the circles that were numbered in the DIC image are the same circles numbered in the IR image. Figure 25 shows the flipped IR image with its resolution and numbered circles, beside the DIC image with the corresponding numbered circles and the resolution.

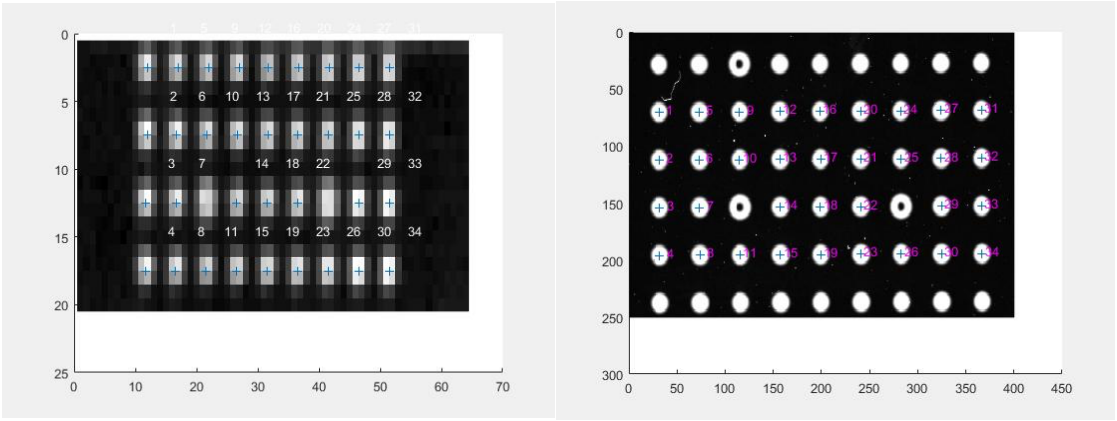

Figure 25: (Left) IR Centers (Right) DIC Centers

The centers of the IR image could then be set over top of the points for the centers of the DIC image by adjusting the *x*, *y*, and *z* coordinates, as well as the pixel count, so that the circles captured in the IR image matched the circles in the DIC image. Figure 26, shows the IR image superimposed on the DIC image with the IR centers identified as blue circles, and the DIC centers identified as red *x*.

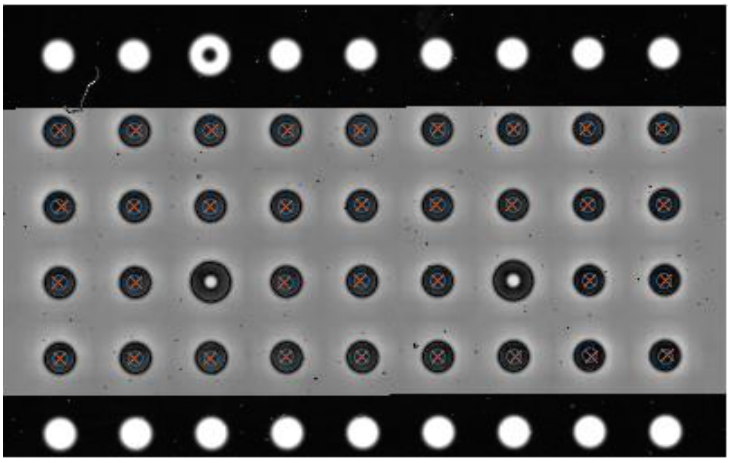

Figure 26: Alignment Centers Overlay

The transformation of the IR image was saved as a MATLAB file that stored the changes made to the image in order to make it match the DIC image. The transformation could then be applied to images from the tests, to overlay the IR data from testing onto the DIC data from testing. This allowed for the temperature values captured by the IR camera for each pixel to be attached to deformation data captured by the DIC cameras for each point. The resulting overlay of temperatures onto the DIC image is shown in Figure 27.

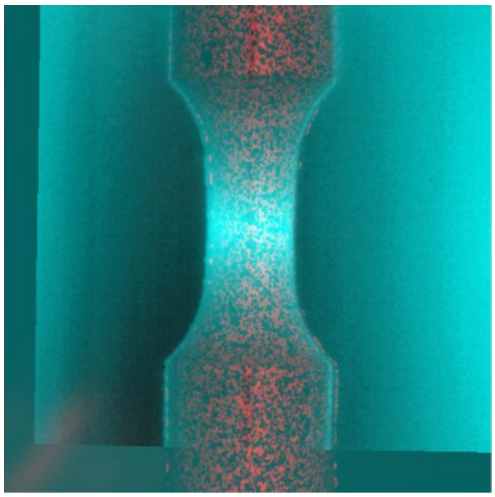

Figure 27: IR Overlay

The result of the transformation of the infrared data was that temperature data points could now be assigned to any data point captured by the DIC cameras. This allowed for a full-field temperature and a full-field deformation data set for a single test. While the IR camera captured full-field radiance it needed to be converted to accurate radiometric temperature and correlated to the DIC data points. A sample of temperatures expanded to the size of the DIC image and transformed can be seen in Figure 28. Here the temperature is in Kelvin.

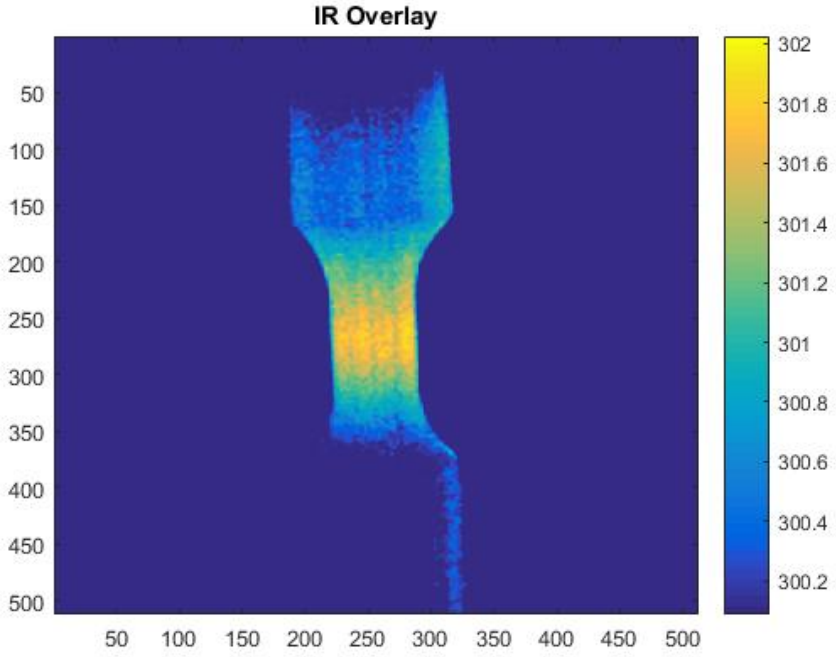

Figure 28: Temperature at DIC points

CHAPTER 3: RESULTS AND DISCUSSION

The current chapter presents the experimental results for the three different strain rate test series, and a comparison of the material response. Data is presented and discussed for each test series focusing on the mechanical and thermal characteristics, including the failure stress, failure strain, temperature change, and any other observed effects affecting material characterization.

3.1 – Mechanical Response

The true stress and true strain curves for all tests can be seen in Figure 29.

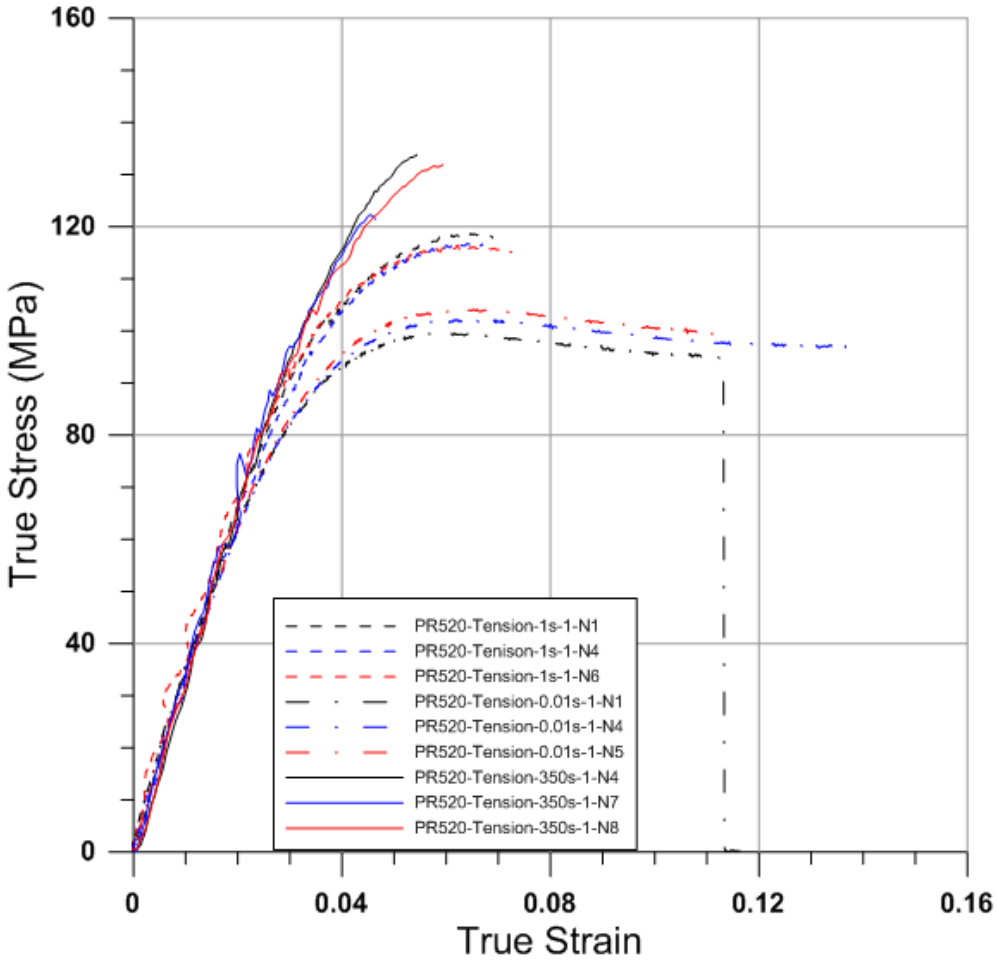

Figure 29: True Stress vs. True Strain for all Rates

From Figure 29 it can be seen that tests at all three rates are repeatable, and the curves at each rate agree with each other. Similarly, the slopes of all curves are similar up to about 1.5 percent strain where the curves start to deviate from each other due to the rate sensitivity of the material. The strain rate sensitivity can be visualized in Figure 30 where the stress for all tests is plotted at both 2 and 4 percent strain.

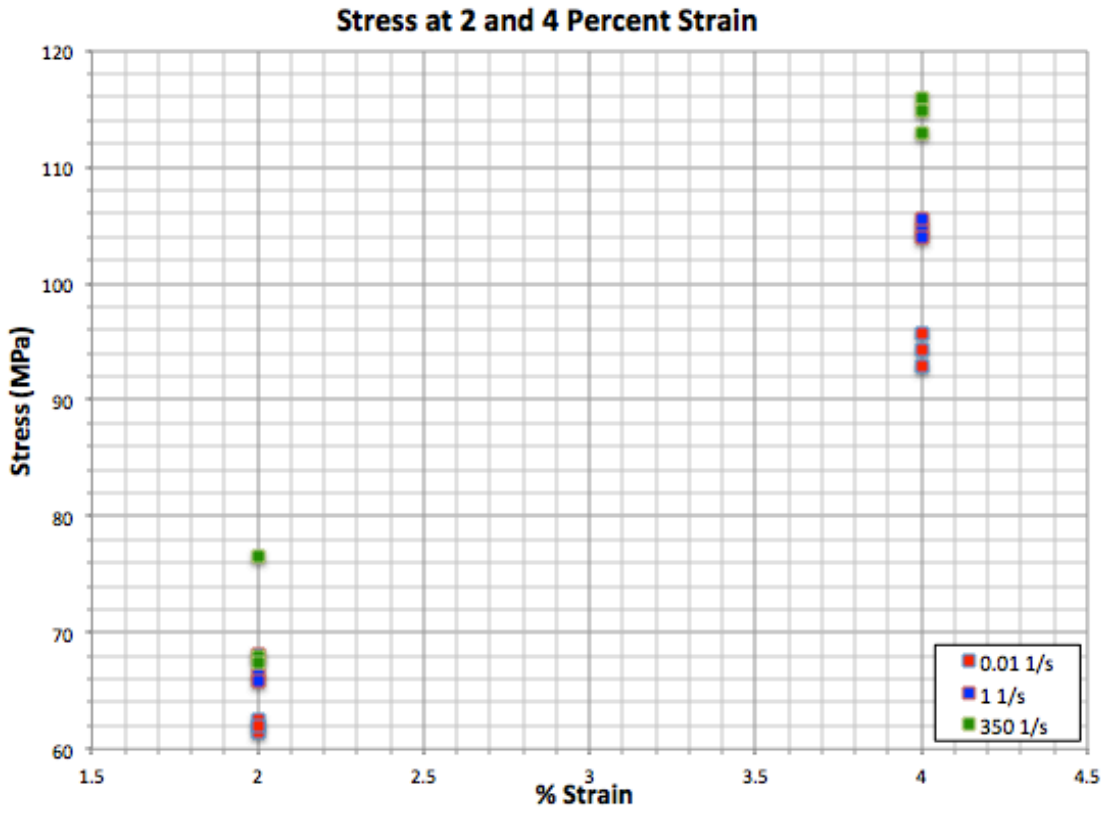

Figure 30: Stress vs. Strain at 2 and 4 Percent Strain

If this plot were continued to 5 percent strain one of the $350s^{-1}$ tests would drop out because it did not reach a strain that high, but the remaining tests would show even larger separation between the three series. It should be noted that as the rate of the testing increases, the material becomes less ductile, but the strength increases. Table 5 outlines

the average failure stress, average failure strain, and the error margins for a 95% confidence interval for each rate.

Table 5: Failure Properties and 95% Confidence Error Margins

Strain Rate	Average Failure σ (Mpa)	Error Margin	Average Failure Strain	Error Margin
0.01 1/s	96.91	2.0611	0.1226	0.01388
1 1/s	116.52	1.09794	0.0697	0.00260
350 1/s	129.06	5.50588	0.0535	0.00598

As the rate is increased from $0.01s^{-1}$ to $1.0s^{-1}$ the failure stress increases by 20.24% and the failure strain decreases by 43.15%. Increasing the strain rate from $1.0s^{-1}$ to $350s^{-1}$, results in a failure stress increase of 10.76%, and a failure strain decrease of 23.29%. It can be concluded that the relation between failure stress and strain rate, and failure strain and strain rate is not linear. This relation can be seen in Figure 31, where the failure stress is plotted against the logarithm of strain rate.

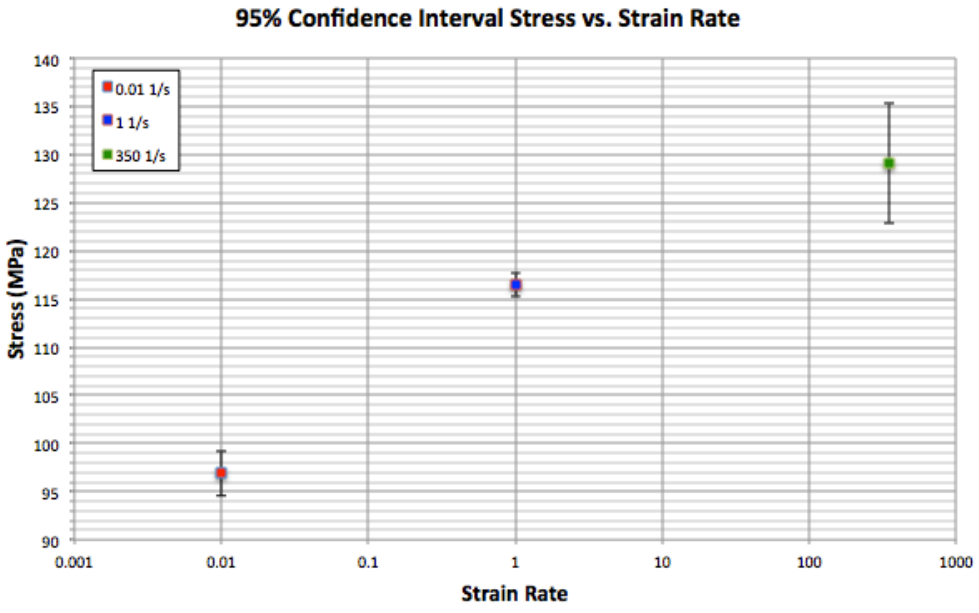

Figure 31: Stress vs. Logarithmic Strain with 95% Confidence Interval

The error bars in Figure 31, represent the 95% confidence interval for the average failure stress at the three strain rates. The fact that none of the error bars overlap demonstrates that the gathered data can be treated as significant, and that variation in results is not due to error in the testing methods.

Another phenomenon worth noting was that for the intermediate and high rate tests, the strain localized in the gage section in bands that would migrate through the gage section. The localizations and movements of the high strain areas led to fluctuations in the load curve that is observed in these tests. The bands of strain localization were insignificant during the $0.01s^{-1}$ tests and the gage had a uniform state of strain. There was no notable difference between the localizations of the $1.0s^{-1}$ test and the $350s^{-1}$ tests. The banded strain localization from failure of a $1.0s^{-1}$ test can be viewed in Figure 32, and the uniform strain at failure of a $0.01s^{-1}$ test can be viewed in Figure 33.

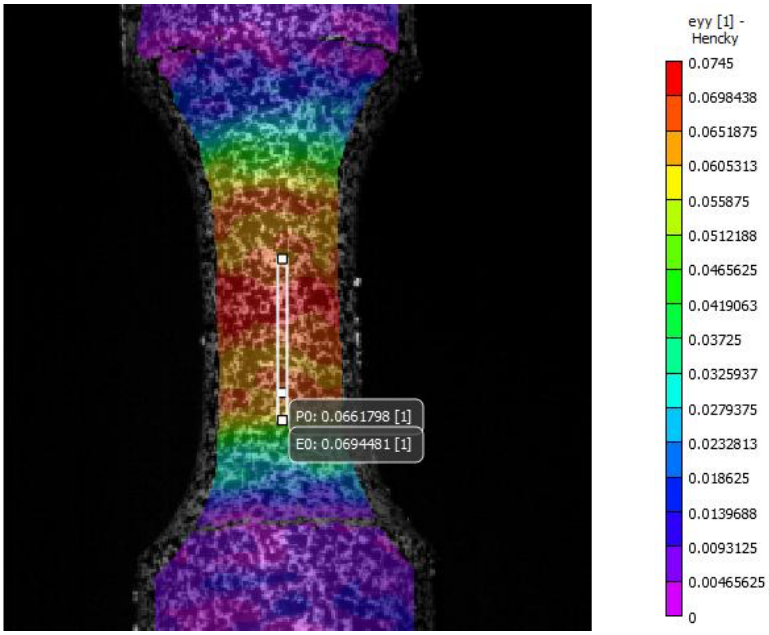

Figure 32: Strain Localization of a $350s^{-1}$ Test

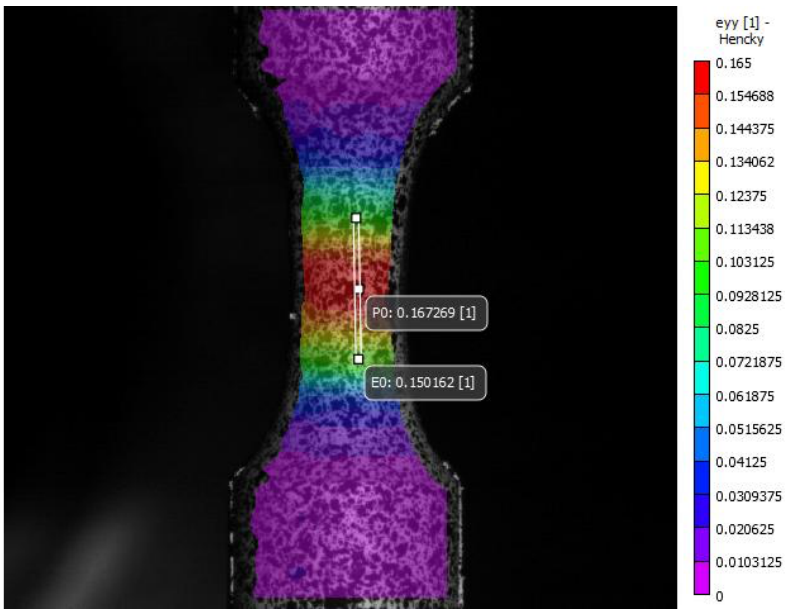

Figure 33: Uniform Strain of a $0.01s^{-1}$ Test

The resulting stress-strain curves for these two tests show how this localization led to fluctuation in the stress. Figure 34 shows the stress-strain curve for the $1.0s^{-1}$ test where the strain localization drives the oscillatory nature of the stress strain curve. Figure 35 shows the stress-strain curve for the $0.01s^{-1}$ test where the gage has a uniform strain.

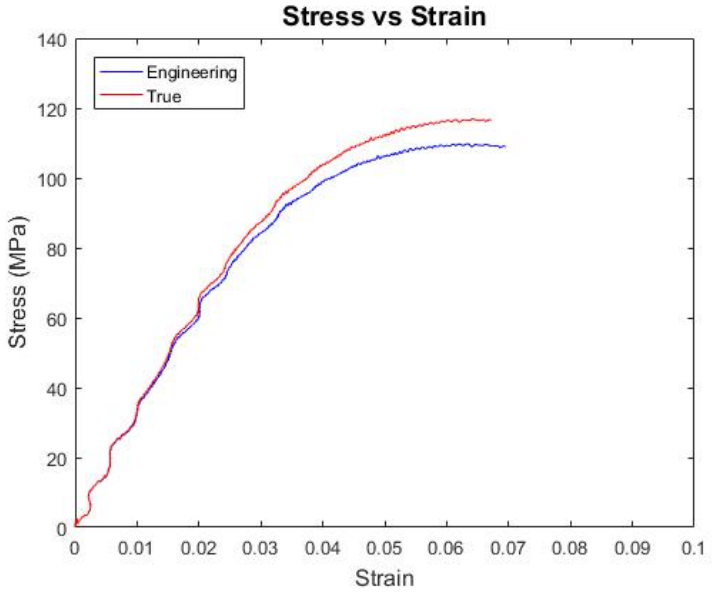

Figure 34: $1.0s^{-1}$ Stress-Strain Curve

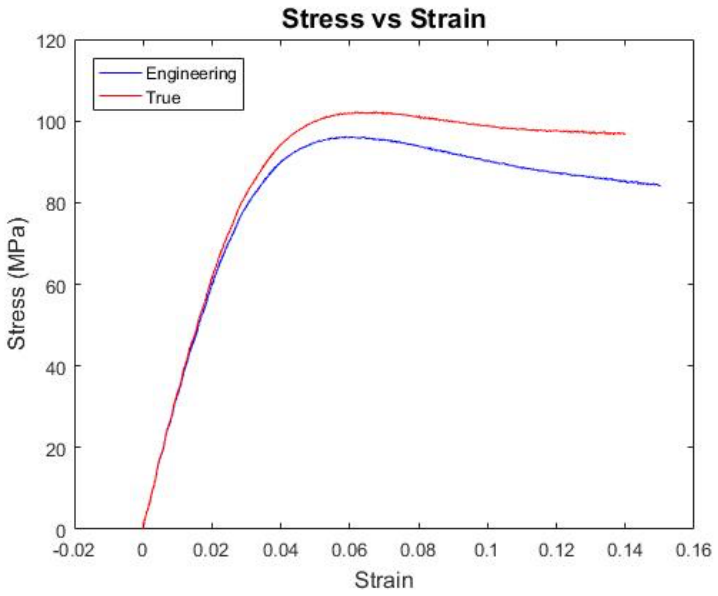

Figure 35: $0.01s^{-1}$ Stress-Strain Curve

Comparing the two curves, it can be seen that at low rates the curve is smooth throughout the elastic region as well as the plastic region. In the $1s^{-1}$ test, the load fluctuates in the elastic region of the loading but then becomes smooth in the plastic region of the curve. This trend is also seen in the $350s^{-1}$ tests as the deformation nearly becomes plastic, but it cannot be stated for certain if this is a phenomenon of high rate elastic deformation on the material. Stress-strain curves for all tests are presented in Appendix A.

3.2 – Thermal Response

Using the infrared camera, temperature changes were captured during testing at all three strain rates. A sample temperature curve for each rate is presented here in Figures 36 through 38.

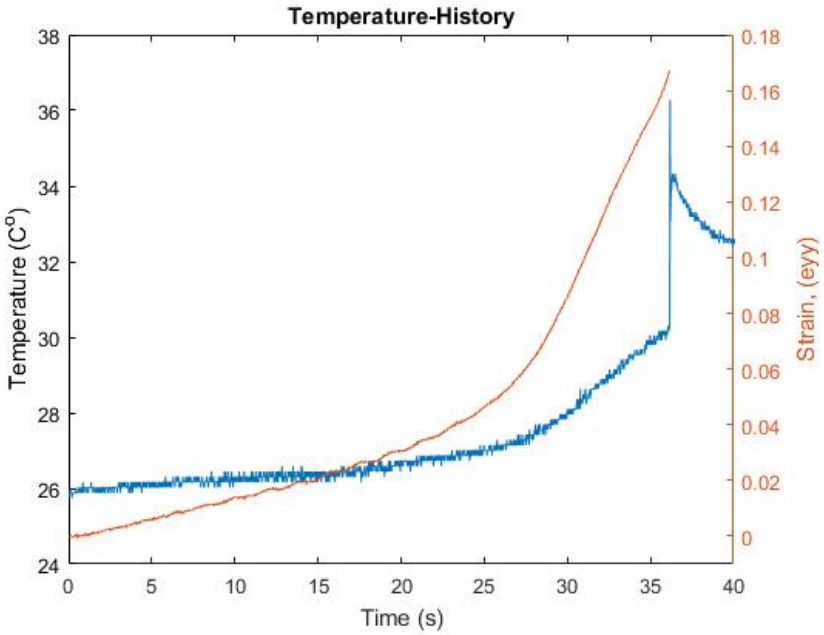

Figure 36: $0.01s^{-1}$ Temperature History

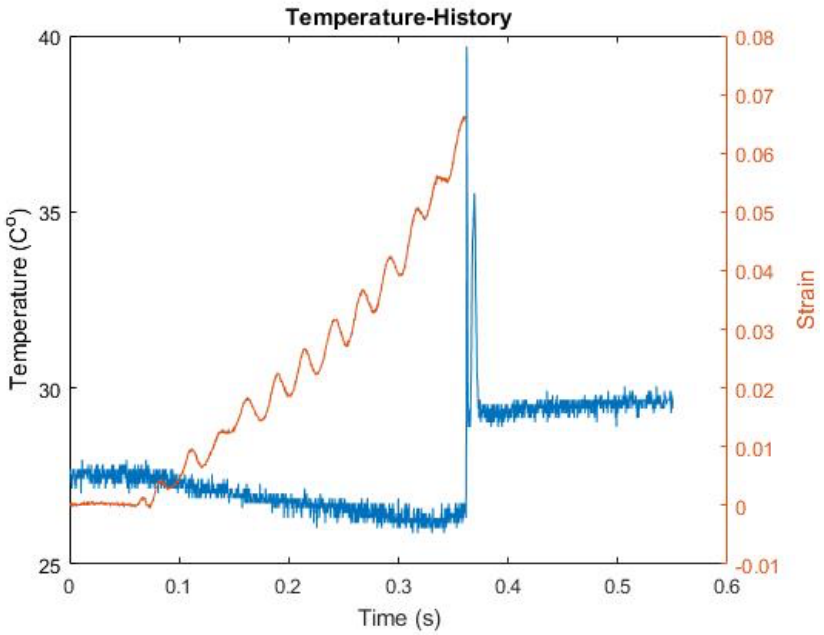

Figure 37: $1.0s^{-1}$ Temperature History

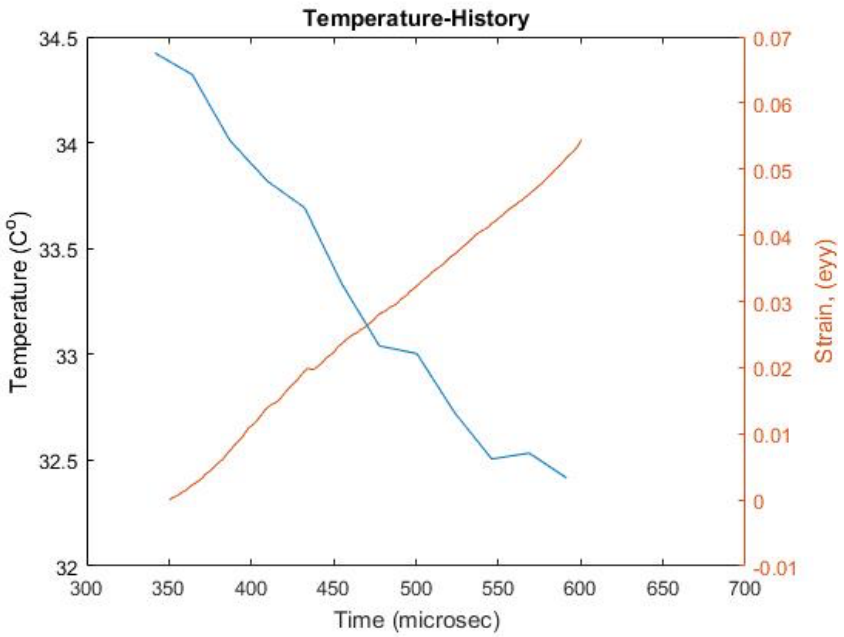

Figure 38: 350s^{-1} Temperature History

The temperature in the 0.01s^{-1} tests showed either no temperature change, or a slight temperature increase, and then a more rapid temperature increase before failure. Examining Figure 29, it can be seen that the inflection point between elastic and plastic deformation occurs around 3% strain for these tests. Referring to Figure 36, the steeper increase in temperature begins when the strain equals 3%. This is to be expected because there will be cooling in the elastic region, and heating in the plastic region. In the elastic region the temperature increases by 1 degree, the specimen temperature then increases by 5 degrees in the plastic region before failure. It would be expected that the temperature should drop in the elastic region, but as was previously discussed, the temperature rise viewed in the elastic region was a direct result of the heating from the light source.

For the 1.0s^{-1} tests, the test duration was short enough that the cooling in the elastic region was captured. Again referring to Figure 29, the inflection point of these tests was around 4% strain, and at this point in the temperature history plot, cooling

ceases and the temperature begins to display a slight rise. However, because the material is becoming more brittle, the specimen fails before any significant heating can occur. The specimen cooled by ~1.5 degree before the heating began and failure occurred.

The same trends that were observed in the $1.0s^{-1}$ tests were repeated in the $350s^{-1}$ tests. However, there was no observable plastic deformation that would lead to any heating of the specimen. The specimen did cool by ~2 degrees during elastic deformation, but because of the rate sensitivity, the material was more brittle than in the previous tests and failed before any plastic deformation could occur. The trends in the temperature change can be better visualized in Figure 39, where the temperature change at 3 different strains is shown for all tests.

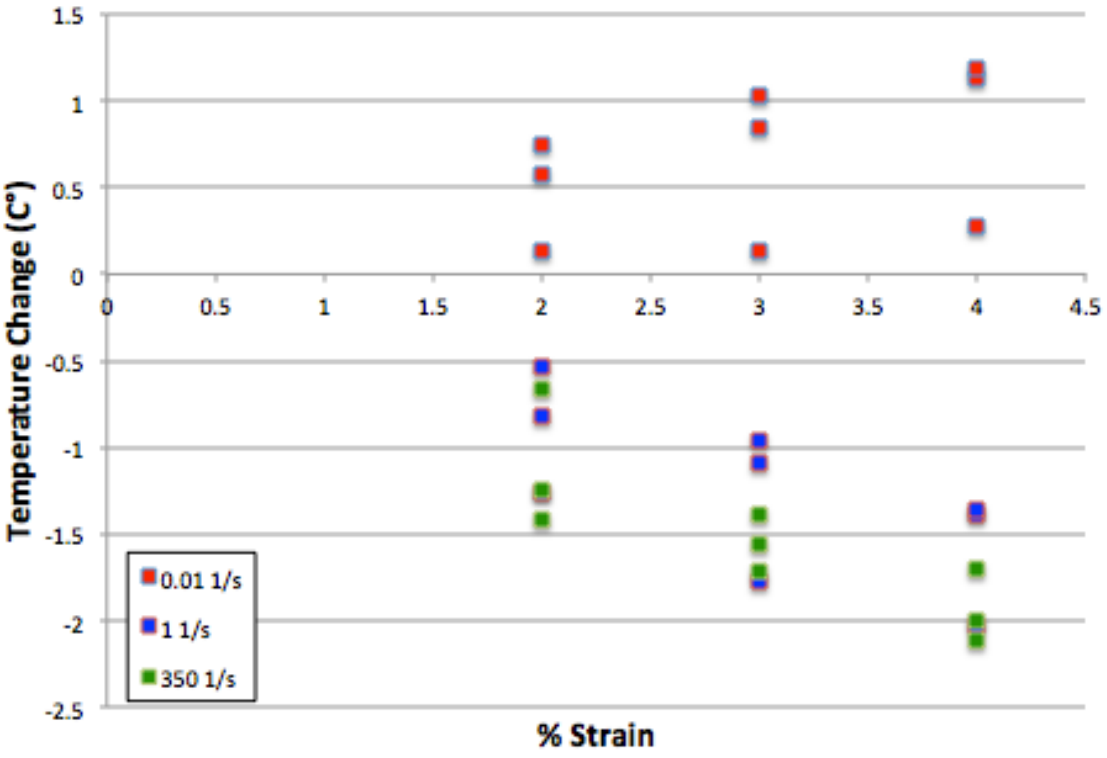

Figure 39: Temperature Change vs. Strain

It should be noted from Figure 39, that aside from the two outliers in the $1.0s^{-1}$ and $350s^{-1}$ tests, the higher the strain rate the greater the cooling at each strain. This plot could be extended to greater strains, but the high rate data would drop out, and the displayed trends would match the temperature-history plots. Due to the heating from the light source, no conclusion can be made about the true cooling of the $0.01s^{-1}$ tests. All temperature plots can be viewed in Appendix B.

An intriguing observation worth noting, is that the two series of tests where strain localization occurred were the two series that consistently displayed cooling in the elastic region. Further work would need to be conducted to determine if there was a correlation between these two responses. Stress vs. Strain and Temperature vs. Strain plots for a test at each strain rate can be viewed in Figures 40 to 43.

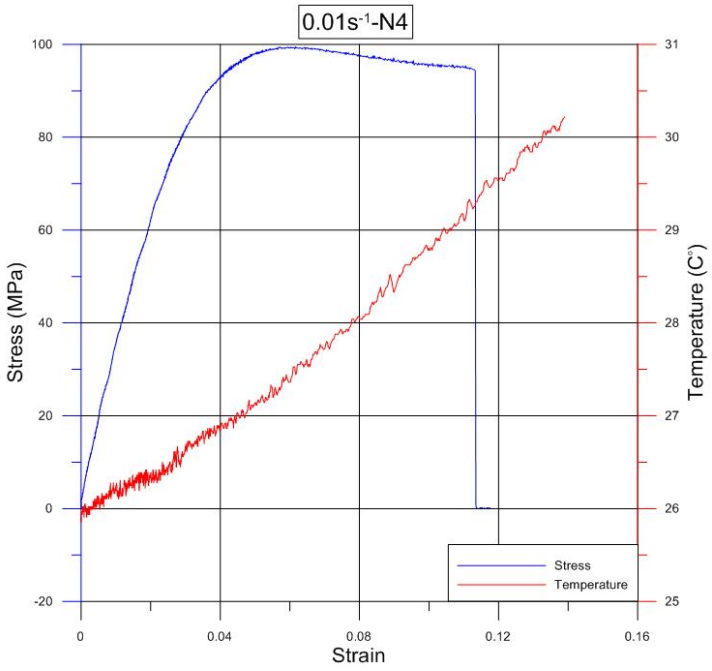

Figure 40: $0.01s^{-1}$-N4 Stress and Temperature vs. Strain

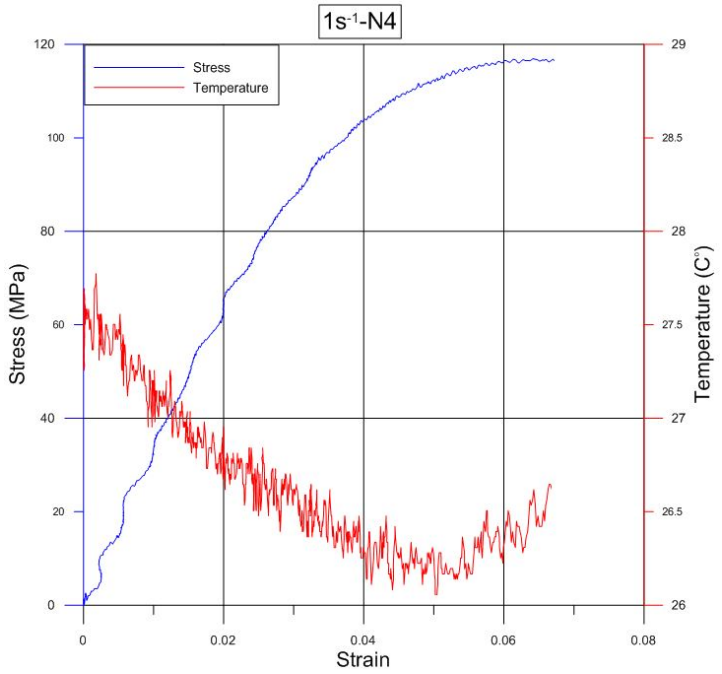

Figure 41: $1s^{-1}$-N4 Stress and Temperature vs. Strain

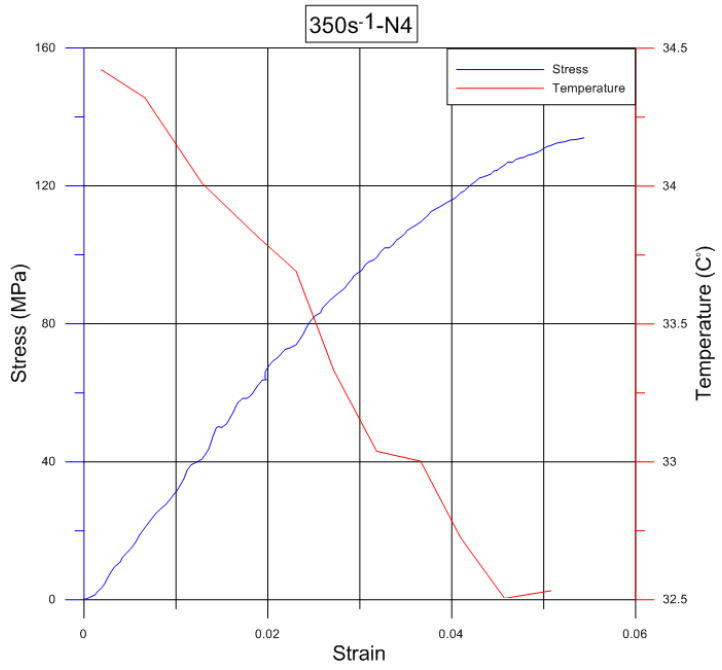

Figure 42: $350s^{-1}$-N4 Stress and Temperature vs. Strain

Looking at Figures 41 and 42, when the temperature drops in the intermediate and high rate test, oscillation in the stress-strain curve occurs as a result of the strain localization in the gage section. As the temperature begins to increase during plastic deformation the stress-strain curves become smooth. In Figure 40 for the low rate test, the temperature steadily increases and the stress-strain curve is smooth. It is possible that the response is due to the strain sensitivity of the material, but it would then be expected that there would be a greater localization in the high strain rate tests, which was not the case. In order to further explore this phenomenon a light source that does not contribute to heating of the specimen would be necessary. However, the light source chosen for this testing was used because it operated at wavelengths undetectable to the infrared camera.

It can be concluded that in impact situations with this epoxy resin, any heating that is observed is not a result of the resin under tensile loading. There are other loading methods that could lead to more plastic deformation of the material and therefore more heating. It will be important to study these loading methods further to fully characterize the material. The material displays clear strain rate sensitivity, and from the temperature results it can be concluded that the magnitude of the thermal response is directly related to the strain rate applied. Further research must be conducted to determine if the heating in the plastic region displays this same relation to strain rate because the brittle nature in tension did not lead to significant plastic deformation at higher rates.

CHAPTER 4: CONCLUSIONS

4.1 – Contributions

The focus of this research was to simultaneously capture the thermal and mechanical response of the epoxy resin PR-520 under tensile loading. Previous work had shown that the methods for capturing simultaneous full-field temperature and strain data could be applied to metals (Seidt et al, 2017), but this was the first application of these methods to PR-520. This was also the first application of these methods for a polymer at high rate, and displayed that a high-speed infrared camera was capable of capturing temperatures at high rate deformations. While the data obtained in these tests was intended to be used to model a composite subjected to impact loading, it was concluded that any observed heating is not the result of tensile loading on the specimen. While this method of loading can be ruled out, further work must be done to determine if other loading methods result in more heating. This work did verify the applicability of these methods to high rate polymer testing, and can be repeated for other materials.

4.2 – Additional Applications and Future Work

The methods used for this study could be applied to nearly any other polymer to capture the thermomechanical response of the material. The only restrictions on this assumption are that the material cannot become significantly more brittle than PR-520 at high rates or the IR camera, at its current capabilities will not be able to capture enough images to construct a meaningful curve. These methods can also be applied to other types of loading provided test apparatus are set up to allow adequate room for camera setup. In order to fully characterize the material, further testing will be conducted using different loading mechanisms. Torsion tests will be conducted at the same rates as were used for

the tension tests, but problems may arise if the specimen deforms out of the view of the camera. In this event, combined shear-tension tests will be conducted at the three rates. Compression tests will also be conducted at the same rates.

4.4 – Summary

This research has presented the results of the thermomechanical response of epoxy resin PR-520 under tensile loading. The results show that no significant heating occurs from tensile loading but there is a strain rate sensitivity that affects the magnitude of the elastic cooling. It cannot be determined if there would be strain rate dependence to the heating occurring during plastic deformation, and further testing may reveal this. The mechanical response of the material is strain rate sensitive, and as the strain rate is increased the material becomes more brittle, but also stronger. The material becomes brittle at over twice the rate as the rate it strengthens. In order to get better data in low rate tests a light source is required that will not heat the specimen, and in order to capture temperature change in higher rate tests, faster infrared cameras will be required.

Appendix A

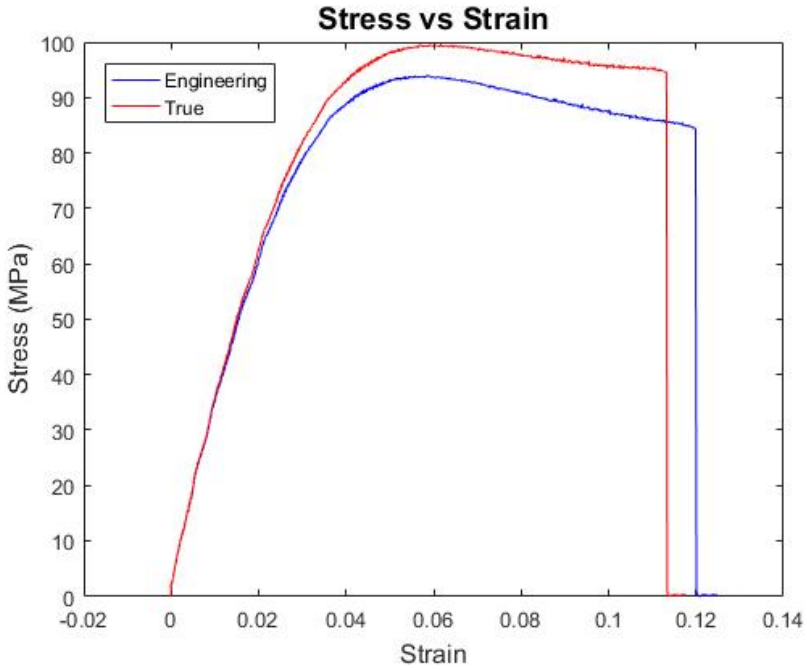

Figure 43: $0.01s^{-1}$-N1 Stress-Strain

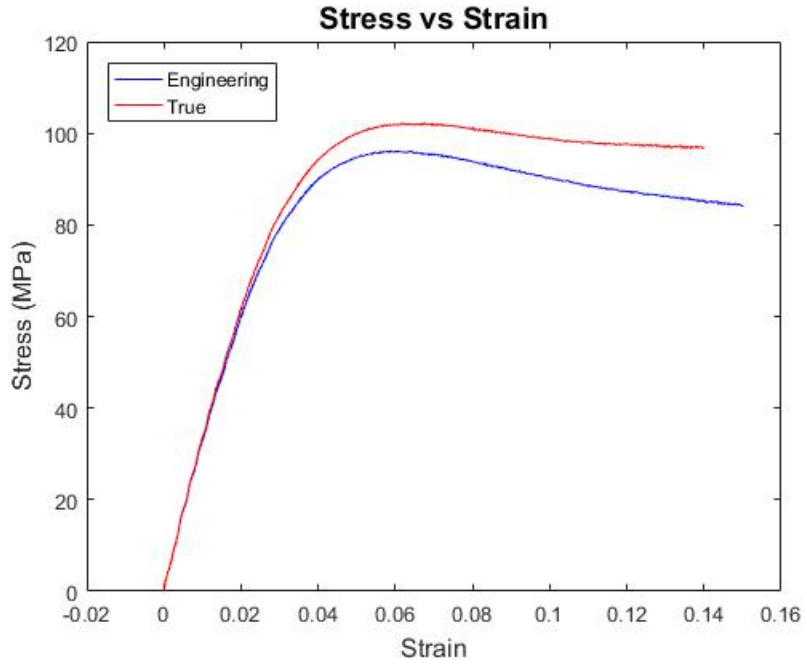

Figure 44: $0.01s^{-1}$-N4 Stress-Strain

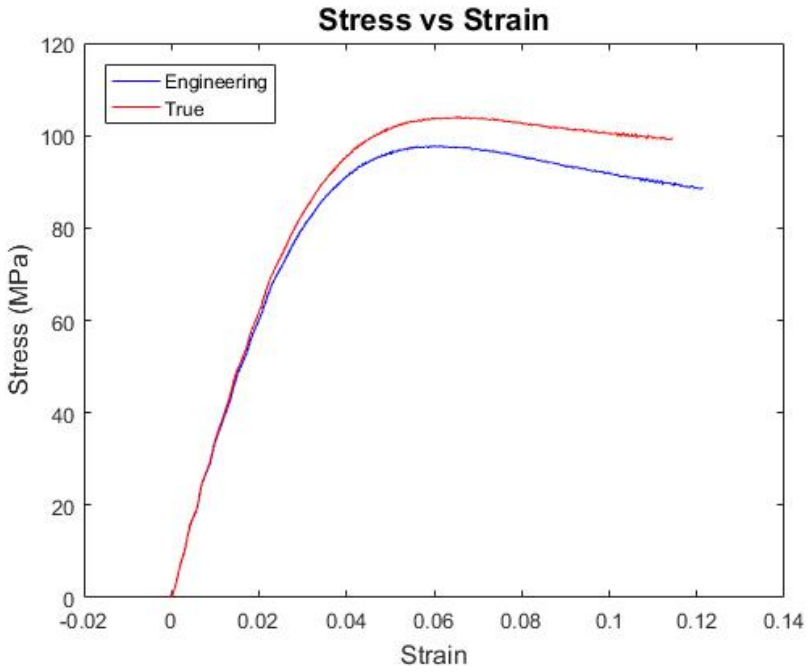

Figure 45: $0.01s^{-1}$-N5 Stress-Strain

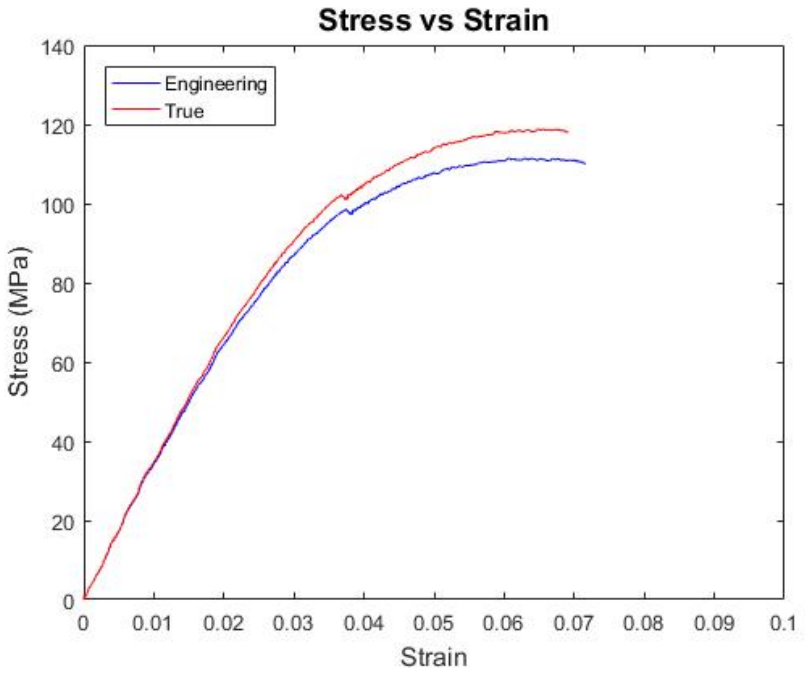

Figure 46: $1.0s^{-1}$-N1 Stress-Strain

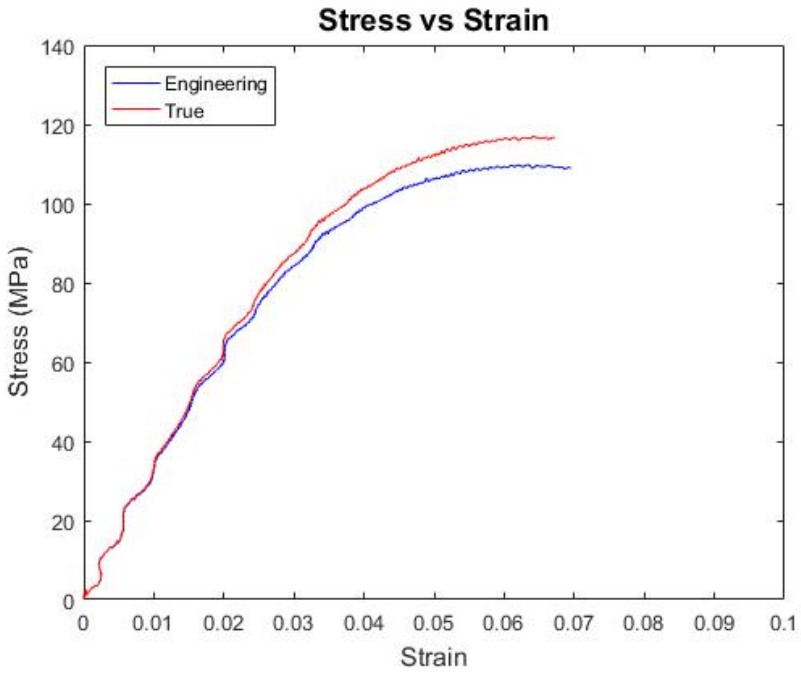

Figure 47: 1.0s^{-1}-N4 Stress-Strain

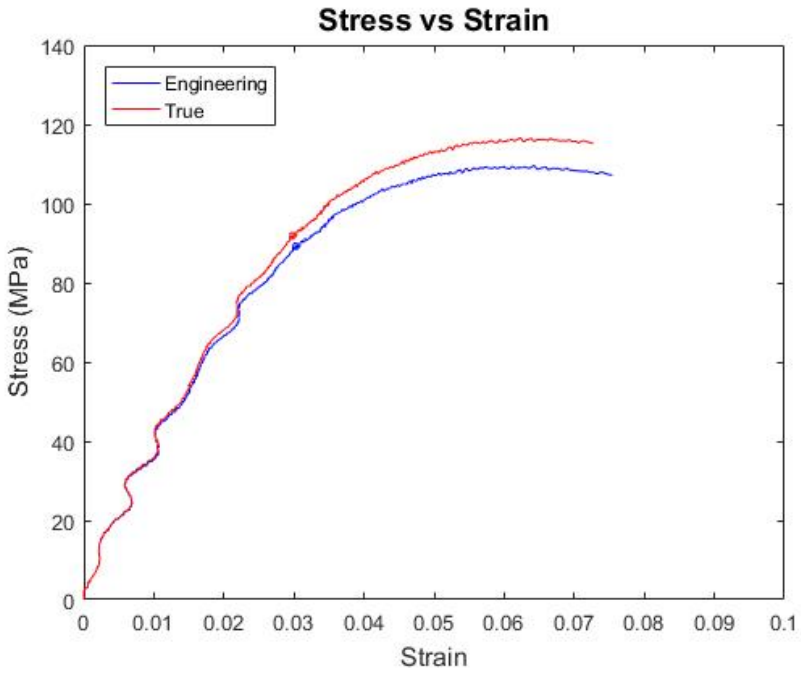

Figure 48: 1.0s^{-1}-N6 Stress-Strain

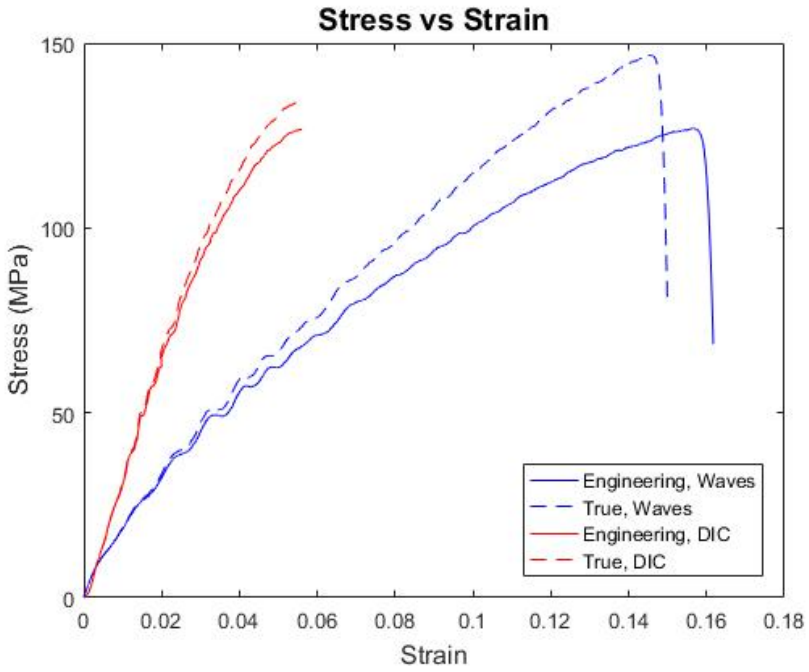

Figure 49: 350s^{-1}-N4 Stress-Strain

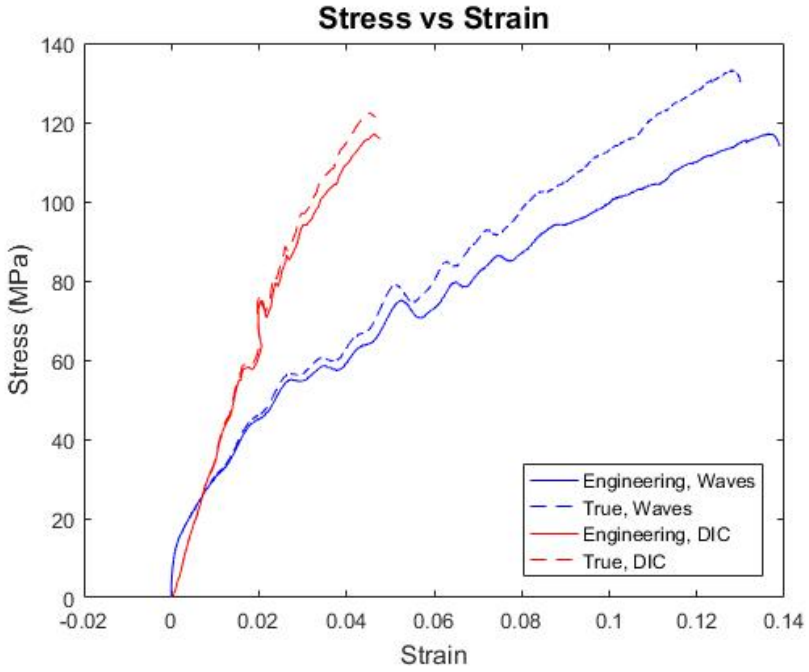

Figure 50: 350s^{-1}-N7 Stress-Strain

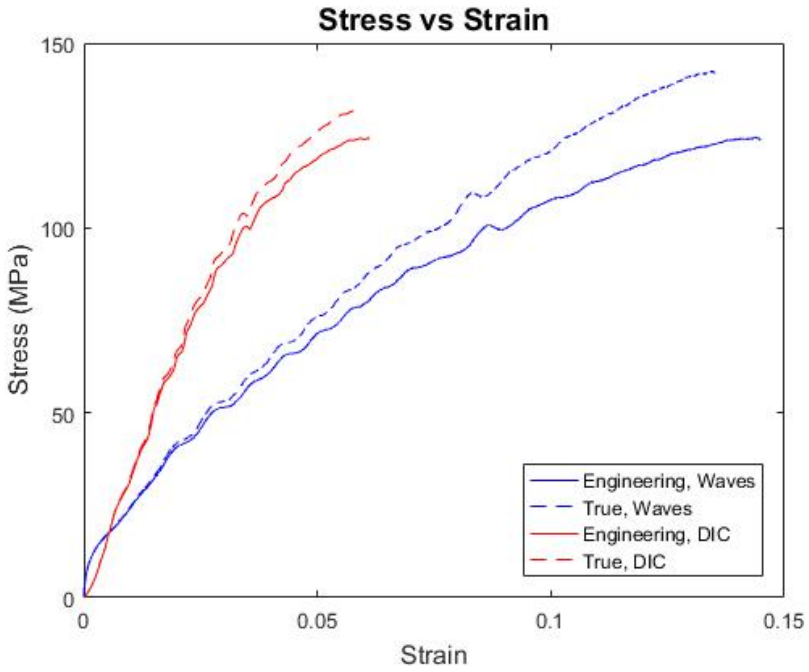

Figure 51: 350s^{-1}-N8 Stress-Strain

Appendix B

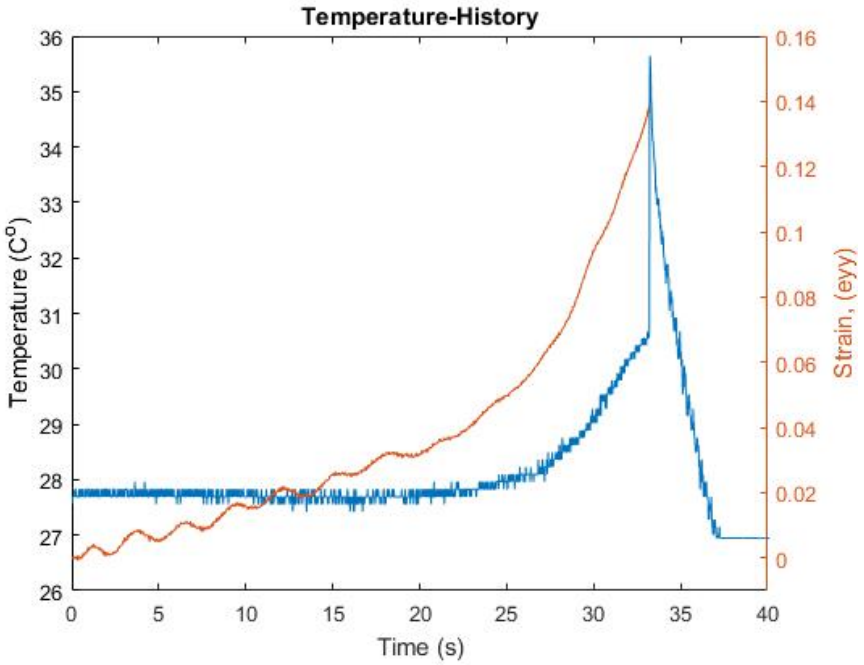

Figure 52: $0.01s^{-1}$-N1 Temperature History

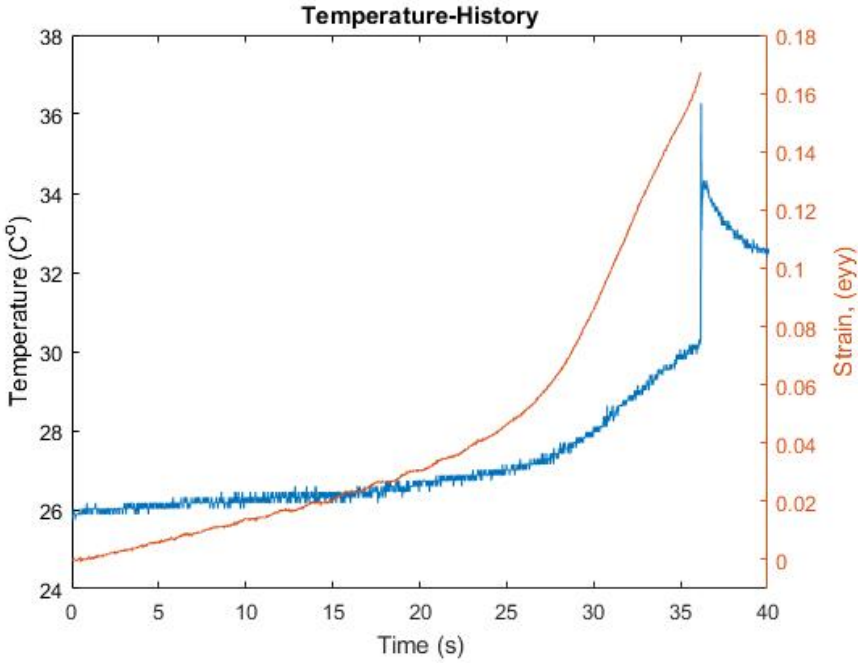

Figure 53: $0.01s^{-1}$-N4 Temperature History

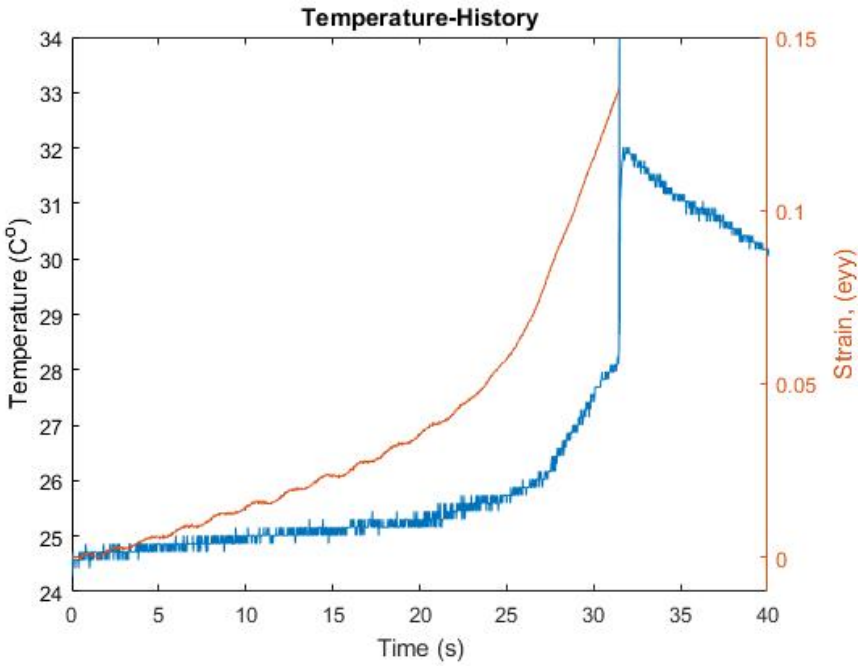

Figure 54: 0.01s^{-1}-N5 Temperature History

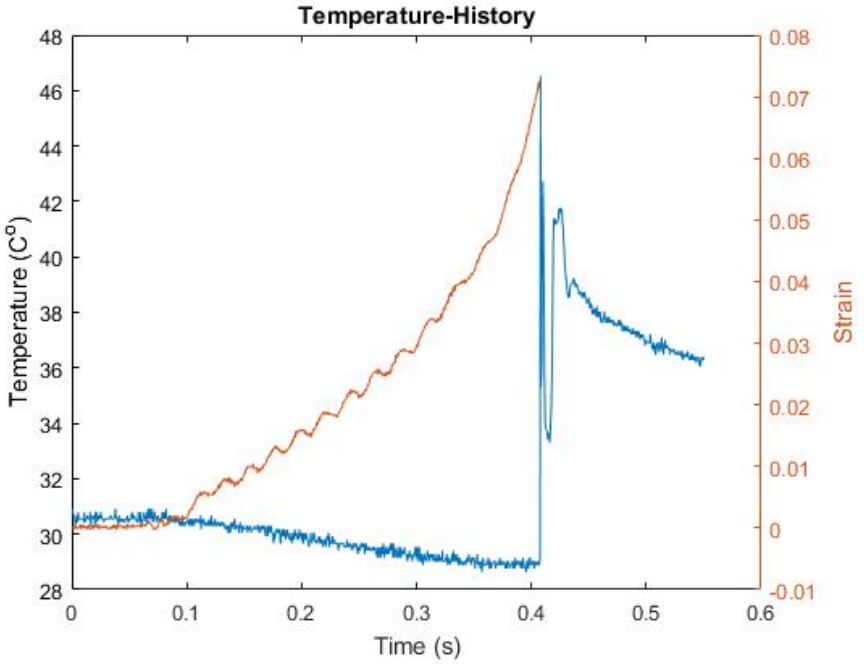

Figure 55: 1.0s^{-1}-N1 Temperature History

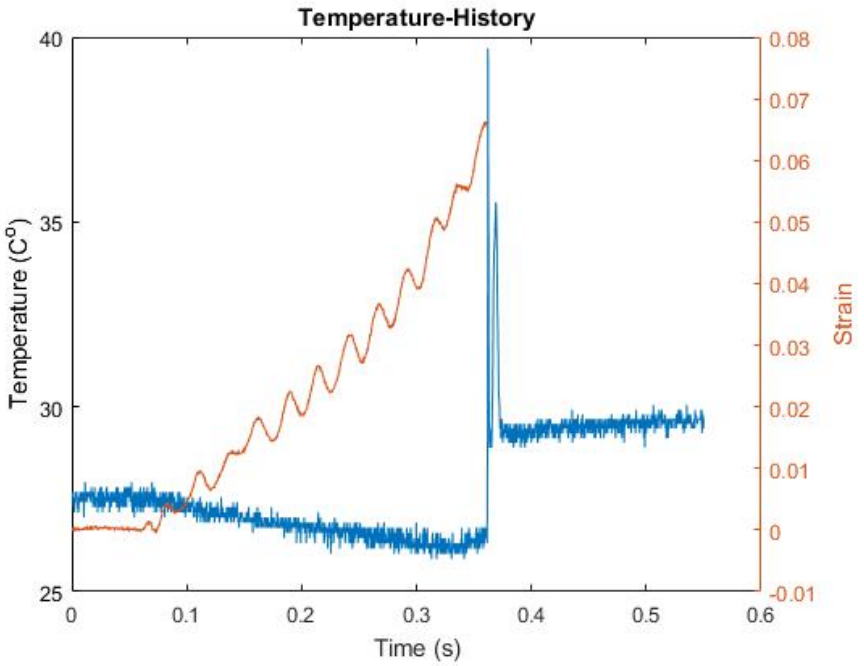

Figure 56: 1.0s^{-1}-N4 Temperature History

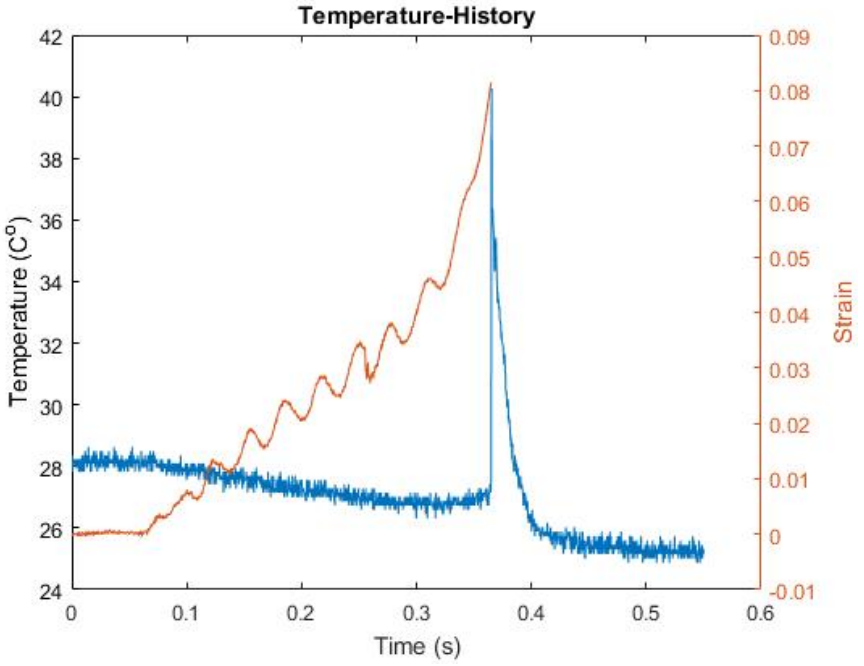

Figure 57: 1.0s^{-1}-N5 Temperature History

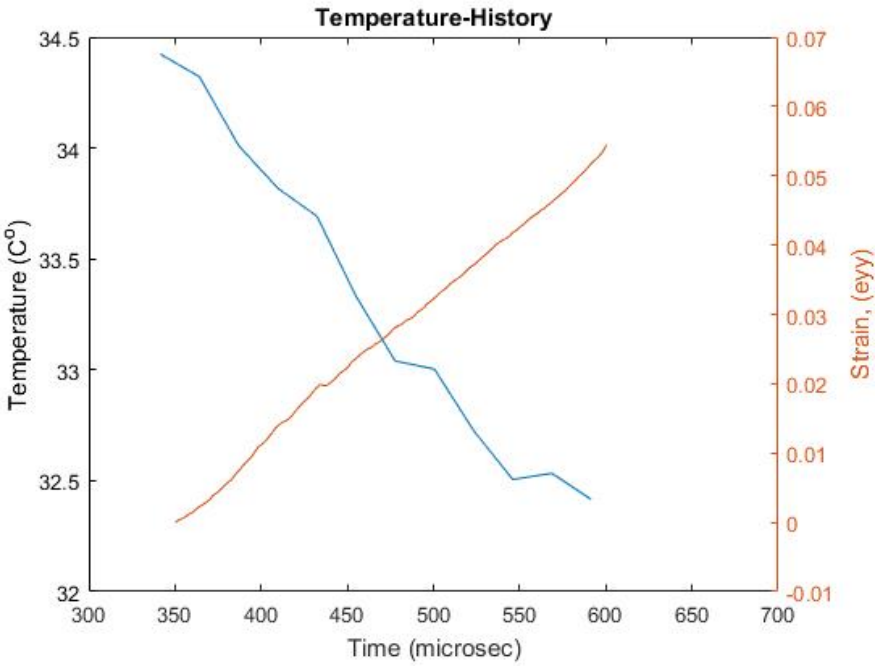

Figure 58: 350s^{-1}-N4 Temperature History

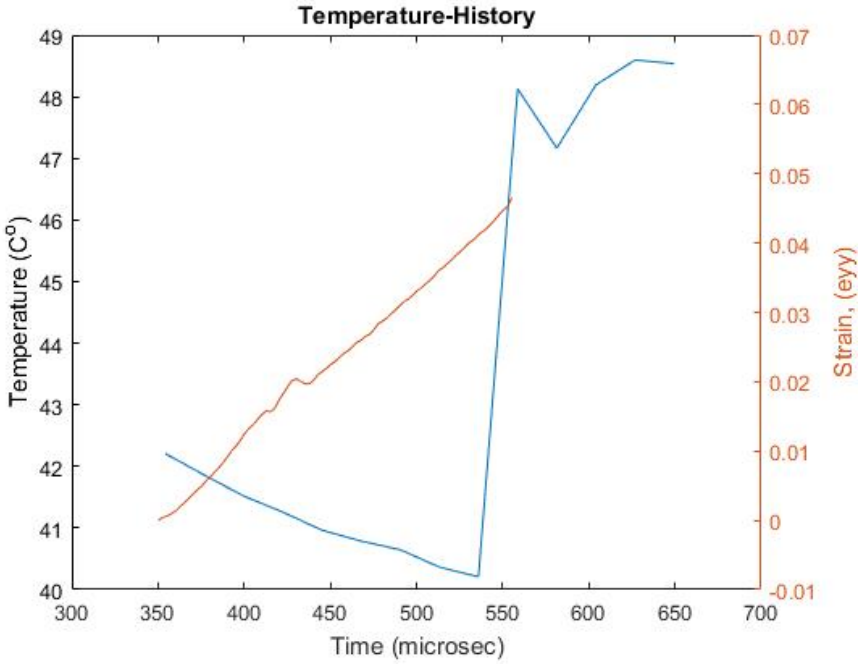

Figure 59: 350s^{-1}-N7 Temperature History

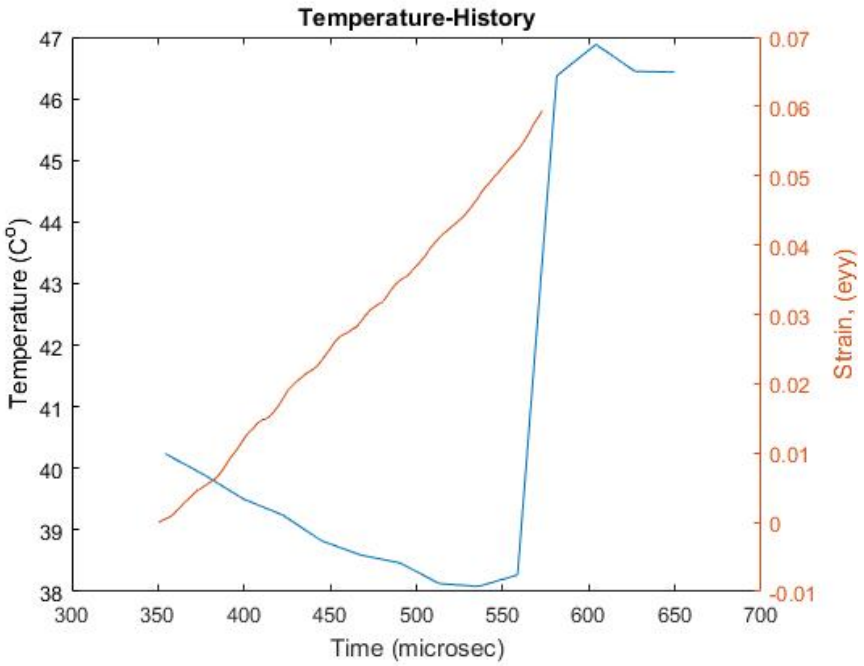

Figure 60: 350s^{-1}-N8 Temperature History

References

1. Anwander, M., Zagar, B.G., Weiss, B., Weiss, H., 2000. Noncontacting strain measurements at high temperatures by the digital laser speckle technique. Experimental Mechanics 40, 98-105.

2. Boeing. 787 Dreamliner Fact Sheet. http://www.boeing.com/commercial/787/by-design/#/advanced-composite-use. Accessed 12-19-2017.

3. Cholewa, N., Summers, P.T., Feih, S., Mouritz, A.P., Lattimer, B.Y., Case, S.W., 2016. A Technique for the Coupled Thermomechanical Response Measurement Using Infrared Thermography and Digital Image Correlation (TDIC), Experimental Mechanics 56, 145-164.

4. Clifton, R.J., Duffy, J., Hartley, K.A., Shawki, T.J., 1984. On critical conditions for shear band formation at high strain rates, Scripta Metallurgica 18, 443-448.

5. Delta Airlines Flight 1288. Digital Image. *Bold Method*. 16 September 2015. http://www.boldmethod.com/blog/lists/2015/09/uncontained-engine-failures-the-most-notable-acciddents/

6. Federal Aviation Administration. Blade Containment and Rotor unbalance Tests. FAR 33.94. 2017.

7. Federal Aviation Administration, 2012. Advanced Composite Materials. In: Aviation Maintenance Technician Handbook – Airframe, Volume 1. United States Department of Transportation, Federal Aviation Administration, Airmen Testing Services Branch, Oklahoma City, pp. 7-4.

8. Gilat, A., Goldberg, R.K., Roberts, G.D., 2007. Strain Rate Sensitivity of Epoxy Resin in Tensile and Shear Loading. Aerospace Engineering 20, 75-89.

9. Gilat, A., Schmidt, T.E., Walker, A.L., 2009. Full Field Strain Measurement in Compression and Tensile Split Hopkinson Bar Experiments. Experimental Mechanics 49, 291-302.

10. Hodowany, J., Ravichindran, G., Rosakis, A.J., Rosakis, P., 2000. Partition of Plastic Work into Heat and Stored Energy in Metals. Experimental Mechanics 40, 113-123.

11. Kapoor, R., Nemat-Nasser, S., 1998. Determination of temperature rise during high-strain rate deformation. Mechanics of Materials 27, 1-12.

12. Littell, Justin. The Experimental and Analytical Characterization of the Macromechanical Response for Triaxial Braided Composite Materials (Dissertation). 2008

13. Littell, J.D., Ruggeri, C.R., Goldberg, R.K., Roberts, G.D., Arnold, W.A., Binienda, W.K., 2008. Measurement of Epoxy Resin Tension, Compression, and Shear Stress-Strain Curves over a Wide Range of Strain Rates Using Small Test Specimens. Aerospace Engineering 21, 162-173

14. Lyons, J.S., Liu, J., 1996. High-temperature deformation measurements using digital image correlation. Experimental Mechanics 36, 64-70.

15. Ortreu, J-J., Rotrou, Y., Sentenac, T., Robert, L., 2008. An innovative method for 3-D shape, strain and temperature full-field measurement using a single type of camera: principle and preliminary results. Experimental Mechanics 48, 163-179.

16. Post, D., Wood, J.D., 1989. Determination of thermal strains by moiré interferometry. Experimental Mechanics 29, 318-322.

17. Rosakis, P., Rosakis, A.J., Ravichandran, G., Hodowany, J., 2000. A thermodynamic internal variable model for the partition of plastic work into heat and stored energy in metals. Mechanics and Physics of Solids 48, 581-607.

18. Seidt, J.D., Kuokkala, V-T., Smith, J.L., Gilat, A., 2017. Synchronous Full-Field Strain and Temperature Measurement in Tensile Tests at Low, Intermediate and High Strain Rates. Experimental Mechanics 57, 219-229.

19. Summers, P.T., Case, S.W., Lattimer, B.Y., 2014. Residual mechanical properties of aluminum alloys AA5083-H116 and AA6061-T651 after fire. Engineering Structures 76, 49-61.

20. Völkl, R., Fischer, B., 2004. Mechanical testing of ultra-high temperature alloys. Experimental Mechanics 44, 121-127.

21. Qantas Flight 32. Digital Image. *Bold Method*. 16 September 2015. http://www.boldmethod.com/blog/lists/2015/09/uncontained-engine-failures-the-most-notable-accident